# Bifunctional Co-based Catalysts for Fischer-Tropsch Synthesis: Descriptors Affecting the Product Distribution

Angela Straß-Eifert,[a, b] Lars I. van der Wal,[b] Carlos Hernández Mejía,[b] Lennart J. Weber,[b] Hideto Yoshida,[b, c] Jovana Zečević,[b] Krijn P. de Jong,[b] and Robert Güttel*[a]

The conversion of synthesis gas to hydrocarbons in the Fischer-Tropsch (FT) synthesis suffers from a broad product distribution not directly providing high fuel quality. This work, therefore, aims at bifunctional catalysts combining the FT and hydroprocessing (HP) reaction for tailoring the product spectrum. Therefore, we applied a bottom-up synthesis strategy for bifunctional cobalt/zeolite catalysts and investigated the obtained materials by advanced characterizations such as 3D TEM tomography. Based on the results, descriptors are defined for the acidity and the porosity, which are varied by changing the material preparation parameters. The catalytic properties of the obtained materials are studied in FT experiments at industrially relevant conditions (20 bar, 240 and 260 °C) and are correlated to the material properties by means of the respective descriptors. Therefore, the product distribution was analyzed in detail and distinguished between n-paraffins and 1-olefins as typical FT-products as well as paraffinic and olefinic isomers formed in the HP classified in different fractions. It was found that, apart from the acidity, the pore structure plays a vital role in primary and secondary cracking/isomerization reactions. In addition to that, the particular 3D pore structure and thus the individual transport trajectories of the FT products are strongly affecting the cracking and isomerization probability and consequently the product distribution.

## Introduction

Nowadays, the energy transition is an attempt of humanity to alleviate climate change driven by greenhouse gases, especially $CO_2$.[1] To meet the upper limit of the global warming of 1.5 °C according to the Paris Agreement, a fast and significant reduction of the global anthropogenic $CO_2$ emissions is necessary.[2] One of the major fields contributing to the global $CO_2$ emissions is the transport sector (23 %).[3] Therefore, among electric mobility, liquid fuels from renewable energy will play an important role in transportation.[4] Consequently, the power-to-liquid (PTL) approach is widely discussed as it provides an alternative for the production of liquid fuels from renewable electricity, $CO_2$, and $H_2O$.[5] The latter process involves several steps including water electrolysis, reverse water-gas-shift reaction (rWGS), and Fischer-Tropsch (FT) synthesis. In this work, we focus on the FT reaction, where the conversion of syngas (CO and $H_2$) at elevated temperature and pressure leads to a variety of hydrocarbons like paraffins and olefins along with the main co-product water [Eq. (1) and (2)].[6,7]

$$n\ CO + (2n + 1)\ H_2 \rightarrow C_nH_{2n+2} + n\ H_2O \quad (1)$$

$$n\ CO + (2n)\ H_2 \rightarrow C_nH_{2n} + n\ H_2O \quad (2)$$

The exothermicity of the reaction, exhibiting a reaction enthalpy of about $-170\ kJ\,mol^{-1}$ under standard conditions for the main reactions, makes heat removal an important concern and requires long-term stable catalyst materials even at elevated temperatures.[6] One of the main side reactions in FT synthesis is the water-gas shift reaction, converting CO and $H_2O$ to $CO_2$ and $H_2$. The low-temperature FT synthesis is typically operated in a temperature range between 190 to 250 °C and at a pressure of about 20 to 30 bar, where cobalt nanoparticles supported on porous materials like silica or alumina are applied as catalyst materials.[8–11] The advantages of cobalt-based catalysts are the high FT activity, a low water-gas shift activity as well as their selectivity towards long-chain paraffins. The polymerization-like reaction leads to a product distribution following the so-called Anderson-Schulz-Flory (ASF) distribution. Therefore, the selectivity towards the gasoline-range fraction is limited to a theoretical maximum of 45 %.[12,13] The main challenges identified in modern FT synthesis research are catalyst deactivation, due to metal nanoparticle sintering and coking, as well as overcoming the ASF product distribution limitation for the production of liquid fuels, which can be tackled at different length scales as recently postulated by

[a] A. Straß-Eifert, Prof. Dr.-Ing. R. Güttel
Institute of Chemical Engineering
Ulm University
89069 Ulm (Germany)
E-mail: robert.guettel@uni-ulm.de
[b] A. Straß-Eifert, L. I. van der Wal, Dr. C. Hernández Mejía, L. J. Weber, Dr. H. Yoshida, Dr. J. Zečević, Prof. Dr. K. P. de Jong
Inorganic Chemistry and Catalysis
Debye Institute for Nanomaterials Science
Utrecht University
Universiteitsweg 99, 3584 CG Utrecht (The Netherlands)
[c] Dr. H. Yoshida
Department of Nanocharacterization for Nanostructures and Functions
Nanoscience and Nanotechnology Center, ISIR
Osaka University
(Japan)

Supporting information for this article is available on the WWW under https://doi.org/10.1002/cctc.202100270

Güttel and Turek.[6] The broad product distribution can either be narrowed by subsequent processes – like hydrocracking and isomerization – usually performed in a second reactor at temperatures between 250 and 350 °C to obtain the desired liquid fuels.[14] Another approach widely discussed in the literature[15–18] is the direct introduction of a second catalytic function, provided by zeolitic materials, to combine FT and hydroprocessing (HP) in one single reactor. This combination requires a compromise between the optimal conditions for each reaction but was already proven on different scales.[6,16,19–21] One major challenge of this approach is the microporous structure of zeolite materials and the related diffusion limitations within the catalyst material. Becker and co-workers[22] already showed theoretically that transport limitations in FT synthesis can be compensated by the introduction of wide transport pores into the catalyst layer. The authors predicted an improvement of productivity by 47% under conditions being industrial relevant. While the described work relies on the improvement of mesoporous structures, microporous structures are expected to benefit from the introduction of additional transport pores, as well. For example, the group of de Jong[23] reported the successful introduction of a trimodal porosity inside hydrocracking active zeolite Y crystals via a combined acid and base leaching strategy. They proposed that the trimodal pore system is beneficial for fast mass transfer of hydrocracking products from the micropores and suppresses secondary cracking.

The combination of two catalytic functions has been studied in the scientific literature at different scales already. At the reactor scale, early studies have been performed by Schaub et al.,[24–27] where they investigated the performance of several dual-layer and physical mixtures for combined FT synthesis and HP. They concluded that hydroprocessing is strongly influenced by FT conversion and depending on the hydrogenation compound either a dual-layer or a physical mixture configuration can be beneficial. More recently, Zhu et al.[19] investigated the use of a structured bifunctional catalyst, consisting of $Co/Al_2O_3$/monolith substrates coated with ZSM-5 films with controlled thickness. While the monolith serves as a structure providing excellent mass and heat transfer characteristics, the ZSM-5 layer acts as a hydrocarbon hydrocracking and isomerization catalyst. The authors reported higher quantity and quality of gasoline-range products ($C_5$—$C_{12}$). The sequential coupling of FT- and HP-catalyst layers in a microchannel reactor by coating of different foils with the two catalysts (FT: $Co/Al_2O_3$ and HP: Pt/ZSM-5) was investigated by Sun et al.[28] The specialty of this concept is the possibility to separately adjust the temperature in the FT and HP reaction zones. At a constant FT and an increasing HP temperature, the product spectrum is shifted towards shorter chain hydrocarbons, while for a constant HP and an increasing FT temperature the selectivity towards $C_{5\text{-}20}$ products is decreasing. The researchers proposed it is necessary to find a compromise temperature between high CO conversion and high selectivity towards $C_{5\text{-}20}$ products.

On the mesoscale, pioneering work was done by Tsubaki et al.,[29–32] which still continues with recent studies. Li et al.[21] studied zeolite-based micro-capsule catalysts with mesoporous nano-silica shells, impregnated with cobalt before and after the encapsulation with the silica shell. The authors report high selectivities towards short-chain products ($C_1$—$C_4$) and $CO_2$ for the former and a significant improvement of the $C_5$—$C_{11}$ selectivity for the latter material. Javed et al.[33] designed a zeolite based capsule catalyst by encapsulation of Co/ZSM-5 with a microporous silicalite-1 shell to create an additional stay zone for both reactants as well as hydrocarbons inside the channels. The results show high CO conversion and gasoline range hydrocarbon selectivity at low $CO_2$ and $CH_4$ selectivities. Sartipi et al.[34] compared the performance of bifunctional catalysts with physical mixtures and catalysts coated by non-acidic layers. The authors reported that the close proximity between the active phase for FT reaction and hydrocracking is essential to eliminate heavier hydrocarbons, but that the membrane coating induces mass transport resistances, as well. The researchers proposed that the use of mesoporous zeolites in combined FT/HP reactions appears promising for the direct synthesis of liquid fractions from syngas.

The microscale, focusing on the active nanoparticles and their close environment, comes into focus of research in recent years. For example, Flores et al.[35] synthesized Co-based mesoporous H-ZSM-5 materials by hard-templating with carbon nanotubes (CNTs). Therefore, they impregnated CNTs with cobalt prior to hydrothermal zeolite synthesis. The authors reported five times higher FT reaction rates compared to catalysts, where the impregnation step with cobalt follows the synthesis of mesoporous H-ZSM-5 materials. They also found a higher selectivity towards branched isomers and ascribed it to the enhanced diffusion and thus preferred removal from the acidic sites. Another approach at the microscale is the synthesis of cobalt-embedded zeolite crystals as investigated by Liu et al.[12] The research group used a conventional $SiO_2$ supported Co-based FT catalyst as precursor and silica source in hydrothermal synthesis method to embed or confine $Co_3O_4$ into the zeolite crystal. The obtained catalysts present a significantly higher gasoline selectivity and produce more iso-paraffins compared to conventional $Co/SiO_2$ and zeolite supported catalysts. The authors attributed this observation to the confined reaction environment, the high diffusion efficiency, and the suitable acidic properties. Carvalho et al.[36] impregnated a zeolite material with cobalt salts resulting in cobalt oxide nanoparticles located inside the zeolite pores, as well as at the external zeolite surface. After synthesis, the cobalt oxide was selectively removed from the external surface through the utilization of large heteropolyacid molecules, which are not able to enter the zeolite pores. During FT synthesis at 20 bar and 250 °C significantly higher selectivity to $C_5$-$C_{12}$ branched hydrocarbons was observed, showing a maximum ratio of isoparaffins to n-paraffins of 5.8. The authors concluded an impact of the location of the cobalt nanoparticles within the support material on the obtained product distribution. In contrast, Lee et al.[20] reported hollow zeolite nanoreactors for promotion of uniform nanoparticle formation and inhibition of sintering of active nanoparticles. For this purpose, hollow zeolite ZSM-5 crystals of ~100 nm were synthesized by the preferential dissolution of the ZSM-5 core using an aqueous

sodium hydroxide solution. Afterward, cobalt oxide particles were introduced in hollow zeolite cages and on zeolite crystals via impregnation. During FT synthesis the two catalysts show the same progress of activity and product selectivity over time, while the inhibition of cobalt particle sintering by the nanoreactor structure was proven via *ex situ* TEM of the spent samples. Therefore, the researcher group suggested that sintering is not the major reason for deactivation, but cobalt oxidation, cobalt-support compound formation, and/or coke formation could be more important issues. Unfortunately, the degree of encapsulation of the cobalt particles was not reported, though the presented TEM images indicate cobalt species both at the external zeolite surface as well as encapsulated inside the hollow nanoreactors.

Our concept at the microscale comprises the design of bifunctional cobalt-based zeolite materials with close proximity between the two types of active sites. The materials are synthesized via a bottom-up approach in order to allow for precise control of the cobalt particle size and therefore good comparability of the different catalyst materials in FT synthesis. Kruse et al.[37] demonstrated this concept already and reported high sinter stability for over 1000 h time on stream (TOS), as well as a narrowed FT product distribution. The broad variety of concepts available to tailor the product distribution in FT synthesis by combination with additional catalytic functionality for HP, however, still lacks the correlation of the identified product spectrum with the structural properties of the catalyst material. Therefore, the identification of suitable descriptors, as already introduced in heterogeneous catalysis, would be the basis.[38,39] Those descriptors should be easily accessible by standard material characterization techniques and tunable during the material synthesis in addition to their impact on the product distribution in FT synthesis. From the literature, the pore structure and acidity of the zeolite, as well as the cobalt surface area can be identified as promising candidates,[40] fulfilling the mentioned requirements.

The present contribution consequently aims at experimental validation of those descriptors, by linking the material characterization results with the obtained product distribution. For this purpose, different strategies for zeolite synthesis are applied in order to manipulate the acidity, while providing a certain proximity of active cobalt nanoparticles and acidic sites of the zeolite matrix. Furthermore, the micropore structure of the zeolite crystals was modified with additional mesopores by steam-assisted crystallization and base leaching. The material properties were characterized in detail by transmission (TEM) and scanning electron microscopy (SEM), X-ray powder diffraction (XRD), $N_2$-physisorption, temperature-programmed reduction (TPR), and $NH_3$-desorption ($NH_3$-TPD), as well as quantitative chemical analysis. In addition, electron tomography investigations were conducted to elucidate the degree of cobalt particle encapsulation and the accessibility of the cobalt particles as well as the connectivity of the pore systems. Finally, FT experiments were performed at industrially relevant conditions to determine the product spectrum for various catalyst materials. The results obtained from material characterization and catalytic experiments were critically discussed in relation to each other, in order to validate the pore structure and acidity normalized by the cobalt surface area as suitable descriptors.

## Experimental Section

### Catalyst Synthesis

The Co-based catalyst materials were synthesized via a step-wise bottom-up synthesis route, firstly described by Kruse et al.[37] The first step includes the solvothermal synthesis of colloidal cobalt oxide particles (**$Co_3O_4$**), which were subsequently encapsulated with mesoporous, amorphous silica via the Stöber process to yield the core-shell catalyst (**Co@mSiO$_2$**). This material was used as catalyst, as well as precursor and silica source for the synthesis of the bifunctional catalysts. Therefore, the amorphous, mesoporous silica shell was converted into a crystalline, microporous zeolite matrix with embedded cobalt oxide particles via the hydrothermal (**Co@silicalite-1-HT** or **Co@HZSM5-HT**) or the steam-assisted (**Co@HZSM5-SAC**) crystallization route. In the last step, Co@HZSM5-HT was leached in basic media to yield a catalyst with a hierarchical pore structure (**Co@mHZSM5-HT**). Note that the catalyst materials were reduced *in situ* to achieve the active metallic cobalt phase, while after the material synthesis cobalt oxide was present. Nevertheless, the designation was adjusted to the active catalyst material.

For the synthesis of **cobalt oxide** particles, 3.32 g cobalt(II) nitrate hexahydrate (Co-nitrate; >97.7%, Alfa Aesar) and 6.64 g polyvinylpyrrolidone (PVP, MW 1.300.000, high purity grade, Amresco) were dissolved in 375 mL EtOH (96 vol-%, VWR Chemicals) followed by solvothermal synthesis at 180 °C for 3 h in a Teflon-lined autoclave. For the subsequent Stöber process, 50 g suspension of $Co_3O_4$ particles and 1.95 g cetyltrimethylammoniumbromide (CTAB, high purity grade, Amresco) as porogen were dissolved in an ethanol/water (60/40-volume) mixture. The basic condition was adjusted by the addition of 12.4 mL aqueous ammonia solution ($NH_{3aq}$, 30% p.a. ACS, Carl Roth). Serving as silica source 6.40 mL tetraethylorthosilicate (TEOS, for synthesis, Merck) was added dropwise to the reaction mixture under stirring. After a reaction time of 2 h at room temperature, the solids were washed with distilled water three times, collected via centrifugation, and subsequently calcined at 500 °C (heating rate 2 K min$^{-1}$) for 6 h yielding **Co@mSiO$_2$**.

For the hydrothermal zeolite synthesis, a modified procedure based on Liu et al.[12] was used: Co@mSiO$_2$ was dispersed in an aqueous mixture of ammonia ($NH_{3aq}$, 30% p.a. ACS, Carl Roth), aluminum sulfate ($Al_2(SO_4)_3 \cdot x\ H_2O$ (x = 14–18), ACS, 98.0–102%, Alfa Aesar) as Al-source, tetrapropylammoniumhydroxide (TPAOH, 40% w/w aq., Alfa Aesar) as structure-directing agent and sulfuric acid (0.1 M, for analysis, Merck) for adjusting the pH. The reaction mixture for synthesis of **Co@ZSM5-HT** exhibits a molar ratio of 1.0000 $SiO_2$: 0.0047 $Al_2(SO_4)_3$: 0.0295 $NH_4^+$: 0.4285 TPAOH: 0.0218 $H_2SO_4$: 42.5733 $H_2O$: 0.4144 $OH^-$, and for **Co@silicalite-1-HT** 1.0000 $SiO_2$: 0.0295 $NH_4^+$: 0.4285 TPAOH: 0.0218 $H_2SO_4$: 42.5730 $H_2O$: 0.4144 $OH^-$ and is based on the recipe of Kruse et al.[37] After reaction at 175 °C for 30 h in a Teflon-lined autoclave, the solid products were purified three times with distilled water, collected via centrifugation, and subsequently calcined at 500 °C (heating rate 2 K min$^{-1}$) for 6 h. For the synthesis of **Co@ZSM5-SAC** via steam-assisted crystallization according to Machoke et al.,[41] Co@mSiO$_2$ was impregnated with TPAOH with a mass ratio of 3:1 (Co@mSiO$_2$: TPAOH) and dried at room temperature for 20 h. After the addition of aluminum sulfate (ratio 1.0000 $SiO_2$: 0.0046 $Al_2(SO_4)_3$) the material was filled in a small Teflon container, which

was placed inside a Teflon-lined autoclave above 24 mL distilled water. The reaction took place at 110 °C for 72 h. Afterward, the solids were washed three times with distilled water, collected via centrifugation, and calcined at 500 °C (heating rate 2 K min$^{-1}$) for 6 h. Due to the sodium-free synthesis routes, no ion exchange was necessary and the $H^+$-form was directly obtained after calcination.

**Co@mZSM5-HT** is achieved via base leaching of Co@ZSM5-HT. Therefore, 1 g of Co@ZSM5-HT was added to 150 mL 0.1 M aqueous sodium hydroxide solution (≥99% p.a., Carl Roth) and stirred for 15 min at 60 °C. After collection of the solids via centrifugation the $H^+$-form of the zeolite was obtained by ammonia ion exchange treating the material three times in 1 M $NH_4NO_3$ solution (≥98% p.a. ACS, Carl Roth) at 60 °C for 60 min, followed by a second calcination step at 500 °C (heating rate 2 K min$^{-1}$) for 6 h.

The reference catalyst **Co/α-$Al_2O_3$** (already used as reference material in previous studies[42]) was synthesized via incipient wetness impregnation of α-$Al_2O_3$ (BASF, BET area 9 m$^2$ g$^{-1}$; grain size of 75–15 μm). Therefore, an aqueous solution of cobalt nitrate hexahydrate (99+%, Acros Organics) in Milli-Q water for a cobalt loading of 8 wt% was prepared. After pre-drying 2 g of the support material at 80 °C for 1 h under vacuum, a pore-filling amount of the solution of the precursor was added dropwise under stirring after releasing the vacuum. After drying for 12 h at 60 °C overnight in stagnant air the material was calcined in a fixed bed reactor under $N_2$ flow (1 L min$^{-1}$) at 350 °C for 2 h with a heating rate of 3 K min$^{-1}$.

### Material Characterization

The TEM measurements were performed on a *Jeol 1400* microscope operating at 120 kV. For sample preparation, the powder samples were suspended in ethanol under ultrasonication. Afterward, one droplet of the suspension was applied on a graphitized copper grid (200 mesh). For statistical evaluation, the diameter *d* of around 220 particles was measured using the software *ImageJ* for image processing.[43] For cobalt oxide particle size evaluation the particle surface averaged diameters ($d_{3,2}$) were calculated via Equation (3) for the total number *N* of particles counted.

$$d_{3,2} = \frac{\sum_{n=1}^{N} d_n^3}{\sum_{n=1}^{N} d_n^2} \quad (3)$$

These values were used for the calculation of the specific cobalt surface area (CSA) under consideration of $d_{Co} = 0.75\ d_{Co_3O_4}$,[34] and based on spherical geometry and the bulk density of cobalt metal [Eq. (4)].

$$CSA = \frac{6}{\rho_{Co}\ d_{Co}} \quad (4)$$

HAADF-STEM-EDX measurements were performed on a Talos F200X (FEI) microscope, operated at 200 kV, which is equipped with an X-FEG electron source and a Super-X$^{TM}$ EDX detector. The STEM images were acquired with a frame of 20 s. The elemental maps of Co, Si, and Al of 2048×2048 pixels were captured with 5 min acquisition time using Velox software. Scanning electron microscopy (SEM) was conducted at a *SmartSEM Supra 55VP, Carl Zeiss SMT Ltd.* electron microscope with an acceleration voltage of 3–6 kV and the use of an SE2 detector to obtain more details of the surface structure. For sample preparation, the solids were glued with carbon tape to a sample holder.

Nitrogen adsorption and desorption measurements were executed at liquid nitrogen temperature (−196 °C) with a high-resolution *Micromeritics 3Flex* instrument with a special micropore port equipped with a 0.1 Torr pressure transducer. Samples were pre-degassed under vacuum at 300 °C for 4 h. The micropore size distribution was determined by the Horwath-Kawazoe model and the micropore volume, the micropore surface area, as well as the external surface area were calculated via the t-plot method. For mesopore evaluation, the method after Barret-Joyne-Halenda (BJH) was applied. The overall pore size distribution was analyzed via density functional theory (DFT). Brunauer-Emmett-Teller (BET) Rouquerol method was applied for the determination of the surface area. Standard parametrization for $SiO_2$ and zeolites was used for all evaluation models. The $H_2$ temperature-programmed reduction (TPR) was measured on the *Micromeritics 3Flex* instrument, as well. For this purpose, the samples were dried at 120 °C for 30 min in an Ar flow. Afterward, the samples were cooled down to 50 °C, and gas was switched to 10 vol-% $H_2$ in Ar. After baseline stabilization, the temperature was ramped up to 850 °C with a linear heating rate of 10 K min$^{-1}$. Calibration of the $H_2$ consumption during TPR experiments is performed by the well-known single-step reduction of CuO to $Cu^0$, using the experimental procedure described above. Therefore, the obtained integrated TCD signal, proportional to the molar amount of $H_2$ consumed, was calibrated with the amount stoichiometrically required for reduction of CuO.

The elemental analysis of the catalysts was executed at *Mikroanalytisches Labor Kolbe* (Oberhausen, Germany). After drying and acidulation of the samples the Co content was determined by atomic absorption spectroscopy (AAS) with an *AAS Model Analyst 200* from *PerkinElmer*. For the analysis of the Si and Al content, the samples were treated with a so-called Wurzschmitt acidulation and measured with a photometric method at a *UV/VIS Model Specord 50 Plus* from *AnalytikJena*.

Ammonia temperature-programmed desorption ($NH_3$-TPD) analysis was performed using a *Micromeritics AutoChem 2990* instrument equipped with a thermal conductivity detector (TCD). Typically, about 100 mg of the sample was dried in a He flow at 550 °C. Subsequently, the sample was cooled to 100 °C in a He flow. Thereafter, pulses of 10 vol-% $NH_3$/He are contacted with the sample until saturation was reached. The temperature (100 °C) and He flow were maintained for 1 h. Afterward, the sample was heated under He flow to 550 °C at a rate of 10 K min$^{-1}$, while the desorption of ammonia was monitored by the TCD detector.

### Descriptors

In the following, our considerations for defining suitable descriptors are discussed based on transport and reaction rates. Considering the transport rate, the impact of the pore structure on the effective diffusion is rather complex, since the mechanisms of diffusive transport depend on the pore size.[44] As a general trend, however, diffusion is improved for wider pores, while it is hindered for small pores and even depressed by orders of magnitudes for very small micropores.[45] Considering that the porous systems studied in the present contribution consist of micro- and mesopores, we assume that diffusive transport of the formed hydrocarbons is dominated by the latter. According to the discussion above, the mesopore volume, easily accessible by $N_2$-physisorption, is considered as a descriptor for the pore structure (PS). The absolute molar amount of acid sites $n_{acid}$, determined via $NH_3$-TPD, is assumed to be representative for the hydroprocessing activity and used as the descriptor for acidity (AC). The cobalt surface area (CSA), determined from TEM data, is used as a descriptor for FT activity and thus hydrocarbon formation rate, assuming a proportional relation between both. Since the catalyst synthesis strategy provides comparable cobalt particle sizes in all materials, the CSA is comparable as well and is thus used as a reference descriptor for discussion of the experimental results. This approach allows

comparability of the samples with respect to FT product formation rate and thus the deduction of the impact of pore structure and acidity on the obtained product distribution.

### Electron tomography

For the sample preparation, Au-particles of 5 or 10 nm were deposited on a copper grid with parallel bars and an even carbon film. Afterward, a droplet of the catalyst powder suspension was applied as described above for standard TEM experiments. Electron tomography measurements were performed on a Talos F200X microscope (Thermo Fischer Scientific). During the investigation, two kinds of zeolite crystals with respect to their size were examined. For all samples, an image series from −74 to 74° every 2° by tilting the sample holder, was recorded. Small zeolite crystals (200–400 nm) were studied by conventional transmission electron microscopy (CTEM), as the limited attenuation of the electron beam still provided transmission of the crystals, though this particle size is not fully representative for the whole catalyst sample. Typical zeolite crystals (500–2000 nm) were investigated by means of scanning transmission electron microscopy (STEM) in bright field (BF) and dark field (DF) mode operated at 200 kV. The tilt images were aligned by tracking the Au particles while a binning factor of two was applied. For 3D reconstruction, a WBP (weighted back-projection) algorithm in the software IMOD[46] was used.

### Catalytic Performance

The catalytic performance in the Fischer-Tropsch synthesis was evaluated using an *Avantium Flowrence* 16 parallel, continuous flow, fixed bed reactor system. The catalysts (sieve fraction 100–200 μm) were reduced from cobalt oxide to metallic cobalt *in situ* at atmospheric pressure in a 30 vol-% $H_2$ in $N_2$ flow for 8 h at 350 °C (heating rate of 5 K min$^{-1}$). Afterward, the samples were cooled down to a reaction temperature of 240 or 260 °C (5 K min$^{-1}$) in a hydrogen atmosphere. Thereafter, the gas stream was switched to a molar ratio of $H_2/CO = 2.0$ with a volumetric flow rate of 5 mL min$^{-1}$ containing 5 vol-% of the internal standard He followed by raising the reactor pressure to 20 bar. Products were analyzed using an online three-channel gas chromatograph (GC, *Agilent 7890B*). The permanent gases ($H_2$, CO, He, $N_2$, and $CO_2$) were analyzed using a *MolSieve 5A* column (2.4 m, 1/8 inch ID) and a TCD. Hydrocarbons were analyzed with a serial connection of a *GS-GasPro* column (30 m, 0.32 mm ID) and an *HP-Innowax* column (6 m, 0.32 mm ID), and a flame ionization detector (FID). The integrated peak areas were used to determine the gas phase composition using He as the internal standard.

## Results and Discussion

### Material Characterization

Representative TEM and SEM images of the catalyst materials are given in Figure 1 along with the synthesis routes starting with the second synthesis step and Co@m$SiO_2$. The TEM image of the starting material $Co_3O_4$ and the corresponding particle size distribution is given in the supporting information (SI) in Figure S1 and S2. The TEM image of Co@m$SiO_2$ (Figure 1, green) reveals spherically shaped particles and a uniform core-shell structure, as indicated by the schematic drawing. The cobalt oxide cores are encapsulated with a mesoporous silica shell exhibiting a shell thickness of about 50 nm and resulting in an overall size of about 170 nm for the individual core-shell particles (see SI, Figure S3). The corresponding particle size distribution is given in Figure S4 (see SI). The SEM images of the catalyst materials Co@silicalite-1-HT (Figure 1, blue) and Co@HZSM5-HT (Figure 1, red), synthesized via the hydrothermal route with and without the addition of an Al-source, show similar particle structures with zeolite crystals of about 1–2 μm in size and cobalt oxide particles present at the external surface, which is also confirmed by TEM. This is also indicated in the schematic drawing, showing a zeolite matrix with encapsulated cobalt oxide particles and some particles on the external surface. Furthermore, having a closer look at the zeolite crystals some sheet-like structures can be observed on the external zeolite surface. The *ex situ* base leached material Co@mHZSM5-HT (Figure 1, orange) exhibits zeolite crystals of the same size and shape as Co@HZSM5-HT, while also sheet-like structures can be found. The expected additional porosity is indicated in the schematic drawing. A difference in zeolite crystal size is detected for Co@HZSM5-SAC synthesized via steam-assisted crystallization (Figure 1, gold), where crystals with a size of about 5 μm are formed showing three-dimensional growth. Cobalt oxide particles can be found at the external zeolite surface as well. From the SEM images, no porosity can be identified for any material. Altogether, these results are in good agreement with our previous findings.[37,47,48] An exemplary, mechanically cut slice of a zeolite crystal of Co@HZSM5-HT, as well as the corresponding cobalt oxide particle size distributions of all zeolite catalysts, are presented in Figure S5 and S6.

The cobalt oxide particle sizes were determined for all materials by counting at least 220 particles from TEM (mean values see SI, Figures S1-S6 and Tab. S1) as described in the experimental part. In Table 1, the cobalt oxide particle sizes evaluated via TEM with about 37 to 42 nm are slightly larger than those estimated via XRD (see SI, Figure S8), which supports the observation that the cobalt oxide cores are agglomerates consisting of smaller crystallites, as shown in Figure S1. The cobalt oxide particle size of the reference catalyst is about one-third of the other catalyst materials and thus closer to the optimal size range between 6.5 to 13 nm (corresponding to Co particle size of 5 to 10 nm).[49] While for the materials via bottom-up route CSA values between 21 and 24 m$^2$ $g_{Co}^{-1}$ were determined, the CSA of the reference catalyst (Co/α-$Al_2O_3$) shows a significantly higher value of 65.1 m$^2$ $g_{Co}^{-1}$, due to the smaller particle size.

For investigation of the cobalt oxide reducibility and determination of Co mass loading, $H_2$ temperature-programmed reduction (TPR) experiments were performed. In Figure 2, the cumulative molar quantity (black) of $H_2$ consumed during the reduction of cobalt oxide to metallic cobalt and its time derivative (red) are presented as a function of temperature. It is noteworthy that the temperature and time are proportional to each other since the temperature increases with a constant heating rate. The transient $H_2$ consumption profiles indicate two temperature ranges for reduction. In region I, between 200 and 480 °C, two peaks can be detected for all catalyst materials representing the two-step reduction of cobalt(II,III) oxide to metallic cobalt.[50] Noticeably, a lower $H_2$ uptake is detected for

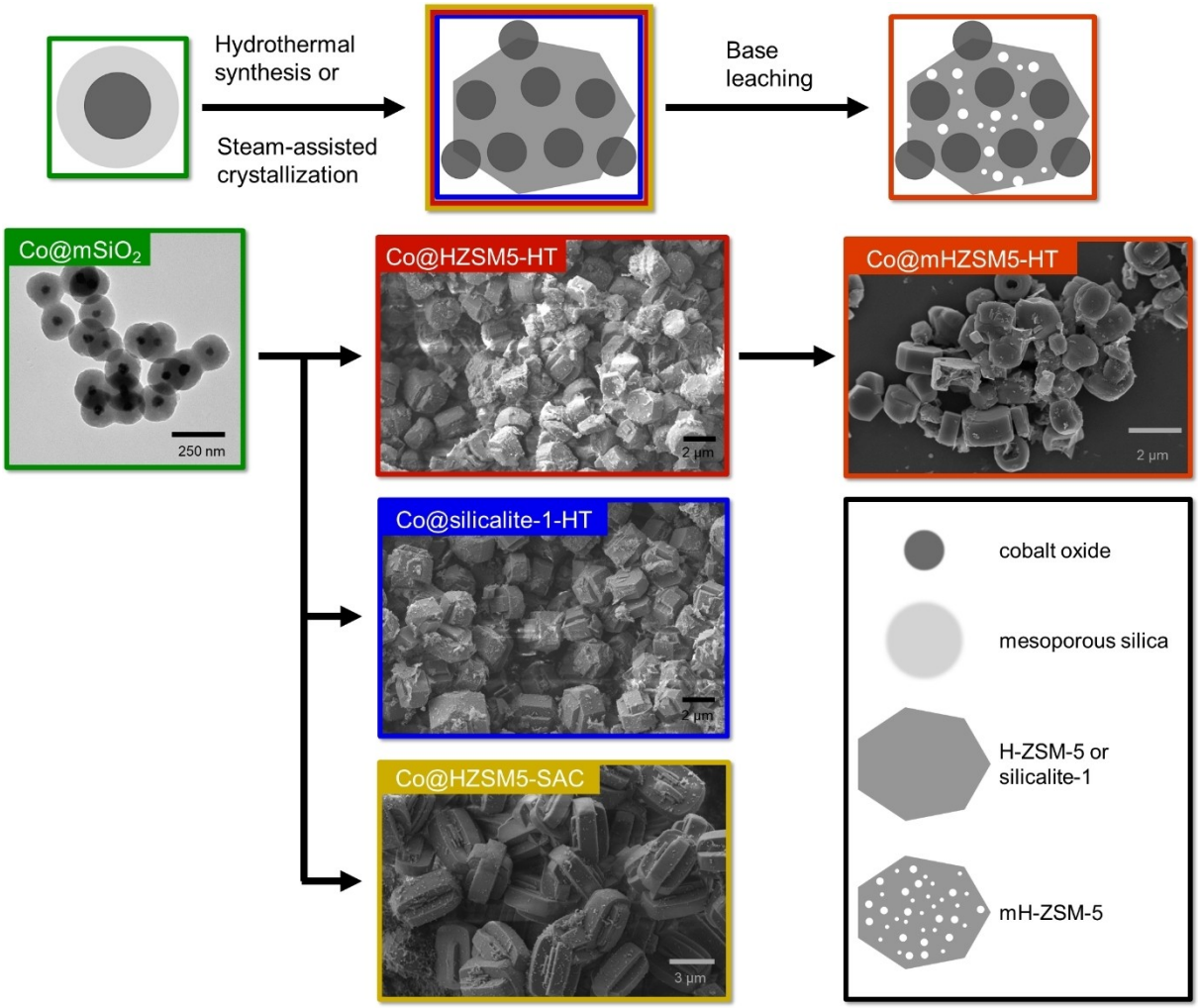


**Figure 1.** Bottom-up synthesis approach; top row: schematic representation of the materials with indication of the respective synthesis routes and the components shown in the legend in the bottom right; bottom row: representative TEM or SEM images of the catalyst materials Co@mSiO$_2$ (green), Co@HZSM5-HT (red), Co@silicalite-1-HT (blue), Co@HZSM5-SAC (gold) and Co@mHZSM5-HT (orange).

**Table 1.** Characterization results of the FT active phase cobalt and the precursor phase cobalt oxide.

| Catalyst | $d_{Co_3O_4}$ [nm][a] TEM | XRD | *CSA* [$m^2_{Co}$ $g^{-1}_{Co}$][b] | $w_{Co}$ [wt%][c] TPR | ICP | $y_{iCo}$ [%][d] |
|---|---|---|---|---|---|---|
| Co@mSiO$_2$ | 42.2[a] | 28.5[b] | 21.3 | 6.8 | 5.8 | – |
| Co@silicalite-1-HT | 39.8[a] | 20.3[b] | 22.6 | 8.7 | 7.1 | 19.5 |
| Co@HZSM5-HT | 36.7[a] | 22.4[b] | 24.5 | 5.9 | 5.0 | 20.3 |
| Co@mHZSM5-HT | 37.1[a] | 31.3[b] | 24.2 | 5.8 | 7.8 | 25.9 |
| Co@HZSM5-SAC | 39.1[a] | 21.7[b] | 23.0 | 6.6 | 4.5 | – |
| Co/$\alpha$-Al$_2$O$_3$ | 13.8[a] | – | 65.1 | 7.7 | 8.0 | – |

[a] size of cobalt oxide particles determined via TEM ($d_{3,2}$) and XRD; [b] specific cobalt surface area calculated from cobalt particle size (TEM); see experimental; [c] total Co content calculated from TPR (region I and II) and determined via ICP; [d] inactive Co fraction determined via TPR (region II).

Co@HZSM5-HT (~0.04 mmol $H_2$) compared to the other catalyst materials synthesized via the hydrothermal route (~0.07 mmol $H_2$), which points to a lower degree of reduction. In region II, between 640 and 820 °C, peaks can only be observed for materials synthesized via the hydrothermal route (Co@HZSM5-HT, Co@silicalite-1-HT, and Co@mHZSM5-HT). For these materials, sheet-like structures are detected in TEM and SEM images, as described above. Therefore, these peaks most probably result from the reduction of Co-phyllosilicates, as seen in previous research.[51–53] Note that Co-species reduced in region II most probably do not contribute to catalysis, since the required temperatures exceed the reduction conditions applied prior to the FT experiment (350 °C, see experimental). The reference material (Co/$\alpha$-Al$_2$O$_3$) exhibits a rather different reduction

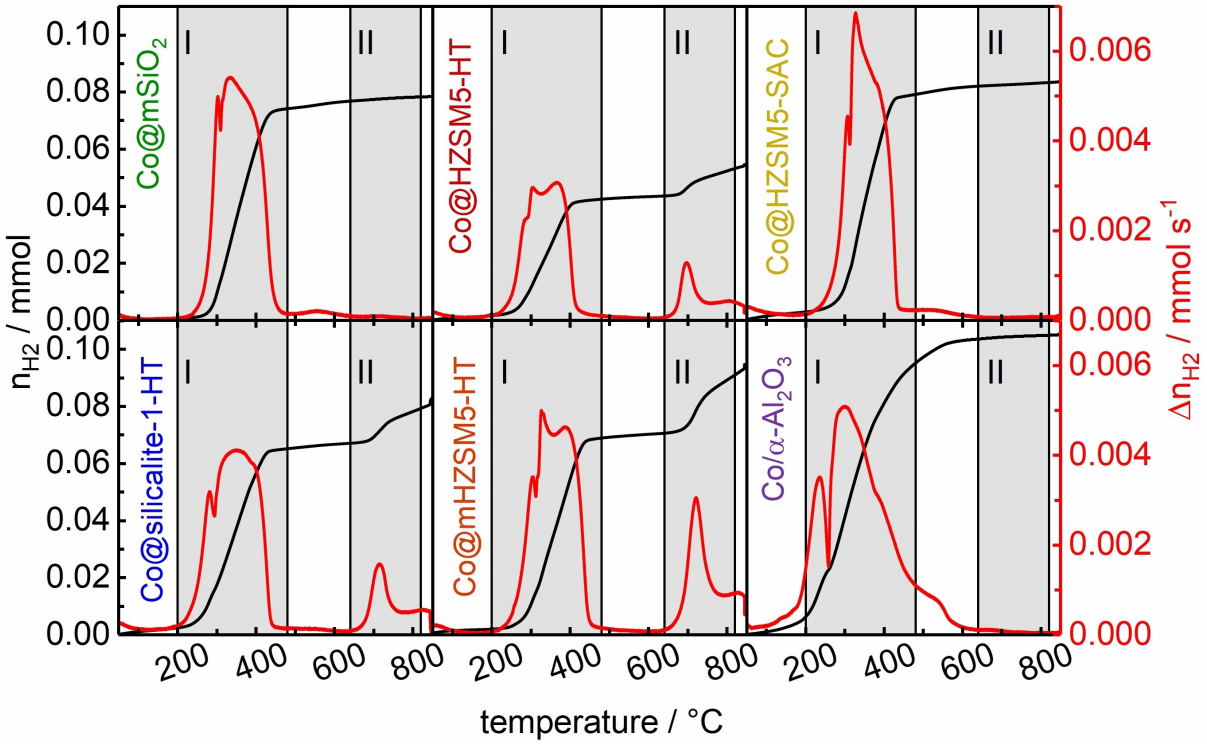


**Figure 2.** Cumulative (black) and transient (red) molar $H_2$ consumption at temperatures from 50 to 850 °C with constant heating rate of 10 K min$^{-1}$; Co@mSiO$_2$ (green), Co@silicalite-1-HT (blue), Co@HZSM5-HT (red), Co@HZSM5-SAC (gold), Co@mHZSM5-HT (orange) and the reference (purple); regions I and II indicate temperature ranges from 200 to 480 °C and 640 to 820 °C, respectively.

profile, most probably due to the interaction between cobalt and alumina.[54] The quantitative evaluation of the TPR profiles by signal integration leads to the total Co content, as well as the fraction of inactive cobalt species (Table 1). The results are compared with the ones achieved by quantitative bulk analysis via ICP. In general, the determined metal loadings with different methods are in good agreement for each catalyst material. Therefore, the accessibility and reducibility of the FT active component within the bifunctional material was proven by means of TPR analysis.

The results of the $N_2$-physisorption measurements are summarized in Table 2. The corresponding isotherms and pore size distributions can be found in the supporting information (see SI, Figure S7). The BET surface area of Co@mSiO$_2$ is at least twice as high as that of the zeolitic materials, while Co/α-Al$_2$O$_3$ shows a comparably small value of 9 m$^2$ g$^{-1}$ (see experimental section). Additionally, no micropore surface area was observed for Co@mSiO$_2$ and Co/α-Al$_2$O$_3$, whereas the zeolitic materials show comparable micropore areas between 248 m$^2$ g$^{-1}$ (Co@silicalite-1-HT) and 317 m$^2$ g$^{-1}$ (Co@mHZSM5-HT). The total pore volume of Co@mSiO$_2$ amounts to 0.66 cm$^3$ g$^{-1}$, while the zeolitic materials exhibit one-third of this value. Assessing the pore sizes, Co@mSiO$_2$ exhibits a monomodal pore size distribution with an average mesopore diameter of 3.2 nm, while Co@silicalite-1-HT, Co@HZSM5-HT, and Co@HZSM5-SAC show a bimodal pore size distribution with micropores of about 0.9 nm and mesopores of 3.2 nm. Here, the micropores are corresponding well to the characteristic size of 0.6 nm of a microporous MFI zeolite. The unexpected and small amount of mesopores observed for all zeolitic materials indicates either incomplete

**Table 2.** $N_2$-physisorption results of all catalyst materials.

| Catalyst | $a$ [m$^2$g$^{-1}$][a] | $A_{micro}$ [m$^2$g$^{-1}$][b] | $V_{total}$ [cm$^3$g$^{-1}$][c] | $V_{micro}$ [cm$^3$g$^{-1}$][b] | $V_{meso}$ [cm$^3$ g$^{-1}$][d] | $d_{micro}$ [nm][e] | $d_{meso}$ [nm][e] |
|---|---|---|---|---|---|---|---|
| Co@mSiO$_2$ | 939 | – | 0.66 | – | 0.66 | – | 3.2 |
| Co@silicalite-1-HT | 330 | 248 | 0.16 | 0.10 | 0.06 | 0.9 | 3.2 |
| Co@HZSM5-HT | 422 | 275 | 0.21 | 0.11 | 0.10 | 0.9 | 3.2 |
| Co@mHZSM5-HT | 475 | 317 | 0.29 | 0.13 | 0.16 | 0.7 | 3.7–26 |
| Co@HZSM5-SAC | 435 | 278 | 0.24 | 0.11 | 0.13 | 0.9 | 3.2 |

[a] BET surface area via Rouquerol plot method; [b] micropore surface area and volume determined via t-plot method; [c] total pore volume determined via adsorbed volume at 0.98 p/p$_0$; [d] mesopore volume determined via subtraction of micropore volume from total pore volume; [e] micropore and mesopore size determined via DFT method.

conversion of mesoporous silica into zeolite crystals or defects within the crystal structure. The leached material Co@mHZSM5-HT, in contrast, exhibits a multimodal pore size distribution offering micropores of 0.7 nm and mesopores in a wide range between 3.7 nm and 26 nm. To confirm the presence of mesopores inside the zeolitic materials and to validate the results additional models were used to process the $N_2$-physisorption data. Therefore, the total pore volume, mesopore size, micropore volume, and micropore size were determined via alternative models, as well (see SI, Table S2). The results are in good agreement with the ones presented in Table 2. In addition to the $N_2$-physisorption results, the XRD pattern confirms the successful conversion of the amorphous silica shell into a crystalline zeolite matrix, which is indicated by a change in the characteristic reflections detected (see SI, Figure S8). As expected for the base leached material Co@mHZSM5-HT a considerable loss of crystallinity due to silicon dissolution was detected, indicated by the decreased intensity of the corresponding reflections.

STEM-EDX analysis was used to determine the presence of Al and the distribution within the zeolite crystals. The corresponding EDX maps, line scans, and spectra of Co@HZSM5-HT and Co@mHZSM5-HT are displayed in Figure 3. In subfigures 1.1 and 2.1, single zeolite crystals of Co@HZSM5-HT and Co@mHZSM5-HT are shown, exhibiting homogeneous Si and Al distribution, while Co displays a more inhomogeneous distribution in subfigure 2.1. A closer look at the line scan over a zeolite crystal of Co@HZSM5-HT (blue line in 1.1) and the corresponding signal profile in 1.2 shows an increasing Si signal (green curve) along the length with a maximum in the center of the zeolite crystal. This observation is probably due to a thicker part of the zeolite crystal or some additional structure behind the zeolite crystal as already visible in the HAADF-STEM image. The Al signal profile (blue line in 1.2) exhibits small fluctuations around a rather constant value. Furthermore, it cannot be excluded that parts of the $mSiO_2$ shell were not fully converted and are still present in the material building a core@shell@shell structure. Nevertheless, the Si/Al ratio seems to be comparable to the zeolite crystal. The line scan of a Co@mHZSM5-HT particle (blue line in 2.1) shows a Si signal profile (green curve in 2.2), which is slightly higher at the surface of the crystal than in the center. The Al signal profile (blue curve in 2.2) shows comparable fluctuations as the signal of Co@HZSM5-HT. The leached material behaves as already described in the literature since silicon is preferably dissolved during the leaching procedure from the regions with most defects probably being within the zeolite core.[55] Surprisingly, no Al was detected for Co@HZSM5-SAC (see SI, Figure S9) pointing towards insufficient or no incorporation of Al during crystallization via the steam-assisted synthesis route. Additional STEM-EDX measurements

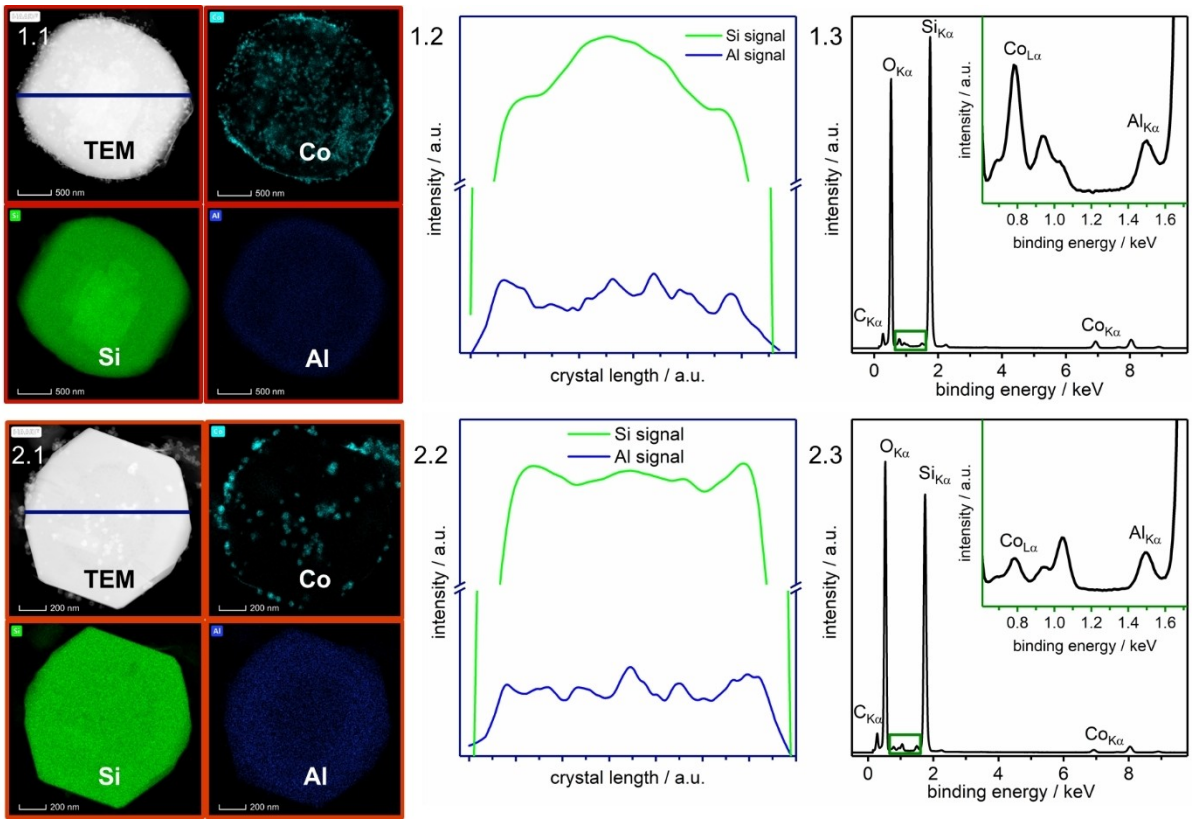


**Figure 3.** STEM-EDX of Co@HZSM5-HT (subfigures 1.1-1.3) and Co@mHZSM5-HT (2.1-2.3); corresponding maps for Si, Co, and Al in green, teal, and blue, respectively, as well as the HAADF-STEM image in the top left, are shown in 1.1 and 2.1; the blue line in the STEM image of 1.1 and 2.1 corresponds to the line scan of Si and Al shown in 1.2 and 2.2; average EDX spectra of a map scan are shown in 1.3 and 2.3 with a green inset providing the details of the region between 0.5 and 1.8 keV; the peak at 1.486 keV is characteristic for Al.

confirm the presence of Co-phyllosilicates in the materials synthesized via the hydrothermal route (see SI, Figure S10).

The bulk composition determined via ICP with respect to Si, Al, and Co, as well as the number of acid sites accessed via $NH_3$-TPD is shown in Table 3. The comparison of Co@HZSM5-HT and Co@mHZSM5-HT shows a decrease in the Si/Al and the Si/Co ratio for the latter. This is consistent since the silicon selective base leaching procedure leads to a decrease in the overall Si content in the sample. The detected increase in the Al/Co ratio for Co@mHZSM5-HT could be a result of the detachment of Co particles from the zeolite crystal during desilication via the base leaching process to generate mesopores within the zeolite crystal. The Al found in Co@silicalite-1-HT, which should be Al-free, indicates Al impurities in the chemicals used causing incorporation of additional Al into the solids. Co@HZSM5-SAC displays an unexpected low Al content, as already found in STEM-EDX measurements, which indicates insufficient Al incorporation during steam-assisted crystallization. The $NH_3$-TPD profiles (Figure S11, see SI) of Co@HZSM5-HT and Co@mHZSM5-HT show two distinct peaks at 185 and 385 °C, which correspond to the desorption of $NH_3$ from weak[56] and strong acid sites,[57] respectively. The quantitative evaluation provides that Co@HZSM5-HT and Co@mHZSM5-HT adsorb the same amount of $NH_3$ ($\approx$0.2 mmol $g^{-1}$) and therefore points towards a similar amount of acid sites. Furthermore, the values detected are also comparable with literature reports on ZSM5 materials.[58] For Co@silicalite-1-HT and Co@HZSM5-SAC, however, no features in the $NH_3$-TPD profile could be detected, which indicates the absence of acid sites for both, as supported by a factor of 10 lower ammonia adsorption capacity. The low acidity for Co@silicalite-1-HT despite detected Al indicates that Al is present as inactive species.

**Table 3.** Results from quantitative analysis and $NH_3$-TPD.

| Catalyst | Si/Al [mol/mol][a] | Si/Co [mol/mol][a] | Al/Co [mol/mol][a] | $n_{acid}$ [mmol $g_{cat}^{-1}$][b] |
|---|---|---|---|---|
| Co@silicalite-1-HT | 302 | 3.62 | 0.012 | 0.02 |
| Co@HZSM5-HT | 318 | 5.59 | 0.017 | 0.18 |
| Co@mHZSM5-HT | 109 | 3.22 | 0.029 | 0.19 |
| Co@HZSM5-SAC | 385 | 5.42 | 0.014 | 0.03 |

[a] atomic ratio determined via ICP; [b] desorbed specific molar amount of $NH_3$ determined via $NH_3$-TPD.

**Table 4.** Descriptors of the physicochemical properties of the catalytic materials (PS: pore structure, CSA: cobalt surface area, AC: acidity).

| Catalyst | *PS/CSA* [$10^{-8}$ $m^3$ $g_{cat}^{-1}$ $m_{Co}^{-2}$ $g_{Co}$] | *AC/CSA* [$10^{-2}$ mmol $g_{cat}^{-1}$ $m_{Co}^{-2}$ $g_{Co}$] |
|---|---|---|
| Co@mSiO$_2$ | 3.10 | 0.00 |
| Co@silicalite-1-HT | 0.27 | 0.88 |
| Co@HZSM5-HT | 0.41 | 7.35 |
| Co@mHZSM5-HT | 0.66 | 7.85 |
| Co@HZSM5-SAC | 0.57 | 1.30 |

### Descriptors

According to the definitions in the experimental section, the descriptors are derived from the pore structure and acidity information obtained from material characterization. The CSA, responsible for the hydrocarbon formation rate in FT reaction, is used as a reference providing the normalized descriptors as summarized in Table 4. The PS/CSA ratio thus corresponds to the relation between diffusion and formation rate of hydrocarbons. It reaches the highest value for Co@mSiO$_2$, which consists of mesopores only and provides the highest pore volume. Among the zeolitic structures, Co@mHZSM5-HT exhibits the highest PS/CSA ratio, as it offers mesopores in addition to micropores. The AC/CSA ratio relates the hydroprocessing activity, expressed by the number of acid sites, with the hydrocarbon formation rate during FT reaction. Obviously, the highest AC/CSA values are found for Co@HZSM5-HT and Co@mHZSM5-HT, being comparable with each other. Both, Co@silicalite-1-HT and Co@HZSM5-SAC exhibit a tenfold lower AC/CSA value being comparable as well.

### Electron tomography

The degree of encapsulation (DOE) of cobalt particles inside the zeolite matrix was determined by 3D transmission electron microscopy (3D TEM), also known as electron tomography since standard 2D TEM images of zeolite slices provide insufficient information on the 3D structure (see SI, Figure S5). Electron tomography provides more 3D data of an intact sample and allows to study the location of the cobalt particles with respect to the zeolite crystal and thus the accessibility, as well. While the spatial resolution is not sufficient in 3D TEM to provide information on the micropore structure, the three-dimensional structure of the mesopores in Co@mHZSM5-HT and the location of cobalt particles can be investigated in detail. The partial encapsulation of cobalt particles inside the zeolite matrix is proven by electron tomography, while the distribution is not homogeneous but completely random (Figure 4, Figure S12 and S13, see SI). For the smaller crystals (200–400 nm) a DOE of about 10% is detected, while the typical zeolite crystals (500–2000 nm) show a DOE between 24 and 34% (see Table 5). Note that DOE refers the number of encapsulated cobalt particles to the total number calculated on basis of Co@mSiO$_2$ particles, necessary for the assembly of the investigated zeolite crystal.

For the sake of clarity, only the 3D images and slices of one representative small crystal are presented in the manuscript to

**Table 5.** Degree of encapsulation (DOE) of cobalt oxide particles in zeolite matrices for small and typical zeolite crystals.

| | small crystal [%][a] | typical crystal [%][b] |
|---|---|---|
| Co@HZSM5-HT | 7.5 | 34.2 |
| Co@mHZSM5-HT | 10.6 | 23.8 |

[a] small zeolite crystal size 200–400 nm, see Figure 4 for 3D TEM results; [b] typical zeolite crystal size 500–2000 nm, see Figures S12 and S13 (in SI) for 3D TEM results.

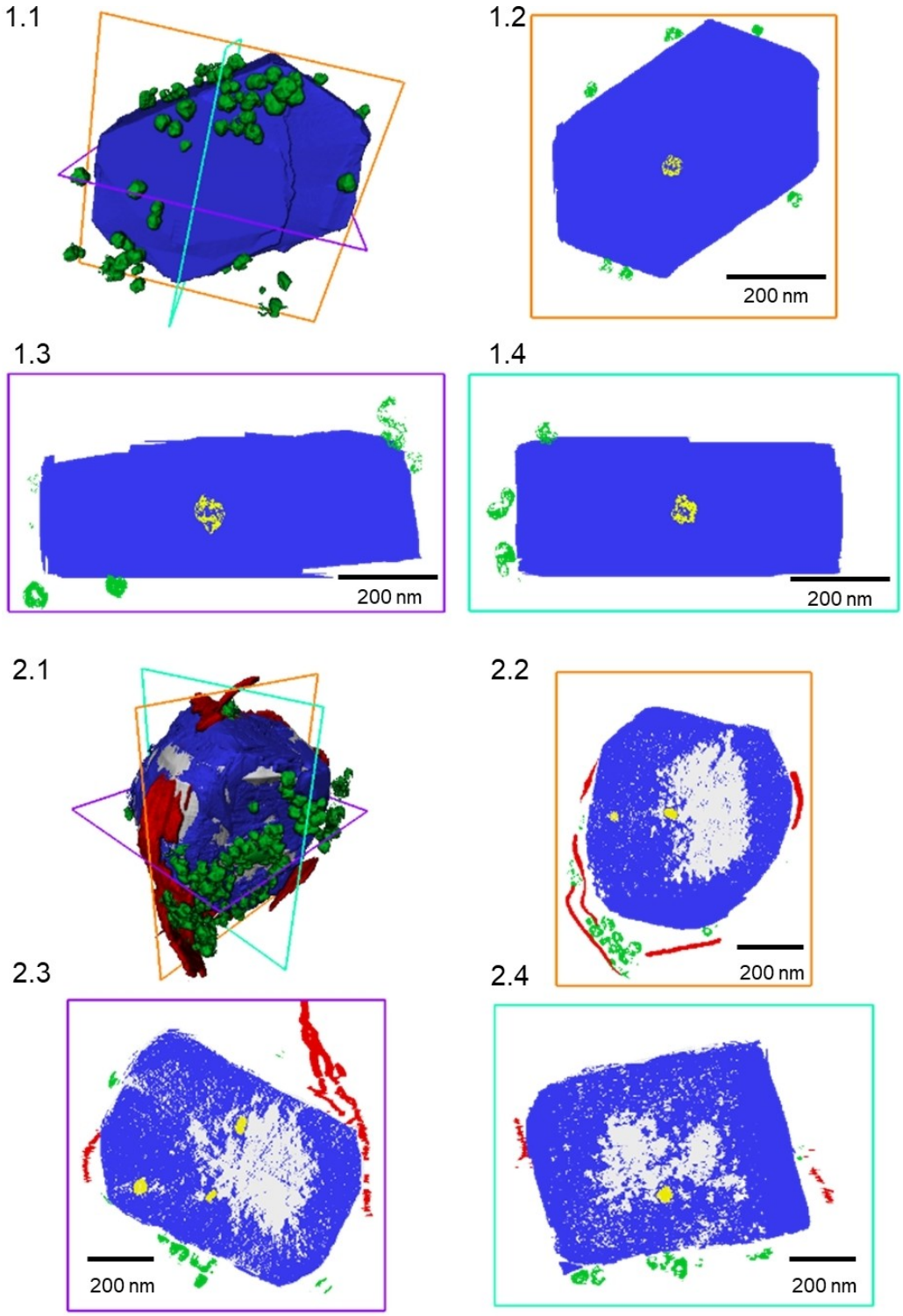


**Figure 4.** 3D images (subfigures 1.2/2.1) and images of slices of xy (1.2/2.2), yz (1.3/2.3), and xz (1.4/2.4) planes of material Co@HZSM5-HT (1.1-1.4) and Co@mHZSM5-HT (2.1-2.4); Co particles at the external surface (green), Co particles encapsulated (yellow) inside the zeolite crystal (blue), cobalt phyllosilicates (red) and pores (white).

show the different aspects in detail (Figure 4). The 3D image and slices through the center of the crystal in xy, yz, and xz direction (Figure 4, subfigures 1.1–1.4) of Co@HZSM5-HT reveal one cobalt particle encapsulated inside the zeolite matrix and randomly distributed cobalt particles attached to the external surface. The encapsulated particle is only accessible through the microporous zeolite structure. As a result of base leaching for Co@mHZSM5-HT (Figure 4, subfigures 2.1–2.4) a cavity in

the center of the zeolite crystal is found, which shows some mesopores reaching the external surface. Interestingly, the cobalt particles inside the cavity are stabilized and accessible via the mentioned mesopores, in addition to the micropore structure. The formation of the cavity during base leaching leads to a significant reduction of the characteristic diffusion length, which corresponds to the thickness of the microporous shell surrounding the cavity. Thus, the accessibility of the cobalt nanoparticles is strongly improved compared to Co@HZSM5-HT. In addition, the abovementioned sheet-like structures, identified as Co-phyllosilicates, are emphasized in red for Co@mHZSM5-HT.

### Catalytic performance

The catalytic performance in FT reaction was evaluated for the different catalysts and the corresponding results are summarized in Table 6. For comparison of the catalytic activity, the CO conversion, the cobalt time yield (CTY), and the turnover frequency (TOF) at both reaction temperatures (240 and 260 °C) were determined and reported (definition see SI, Tab. S3). Note that the CTY corresponds to the cobalt mass-specific reaction rate. The corresponding hydrocarbon selectivities are presented in Figure 5 and Table S4 (see SI). Note that a smaller catalyst mass was used at 260 °C to achieve similar CO conversions at both temperatures investigated. For comparison to conventional FT catalysts of industrial relevance, Co/$\alpha$-$Al_2O_3$ was used as reference at 240 °C.

The values indicate a moderate activity in FT synthesis for all catalyst materials investigated compared to the reference material. In particular, the obtained values of CTY at 240 °C for Co@$mSiO_2$, Co@silicalite-1-HT, Co@HZSM5-HT, Co@mHZSM5-HT, and Co@HZSM5-SAC are in agreement with our own results presented earlier,[37,48] as well as to literature. For instance, Khang et al.[17] investigated impregnated silica and zeolite catalysts at almost the same reaction conditions and reported CTYs of $5.2\cdot10^{-5}$ $mol_{CO}\,g_{Co}^{-1}\,s^{-1}$ and $2.7\cdot10^{-5}$ $mol_{CO}\,g_{Co}^{-1}\,s^{-1}$ for Co/$mSiO_2$ and Co/HZSM5, respectively. Reasonable agreement with the work of Sartipi at el.[34] is also given, considering the differences in reaction pressure, who are reporting $7.2\cdot10^{-5}$ $mol_{CO}\ g_{Co}^{-1}\,s^{-1}$ and $13.0\cdot10^{-5}$ $mol_{CO}\,g_{Co}^{-1}\,s^{-1}$ for Co/$mSiO_2$ and Co/mHZSM5. The results of Carvalho et al.,[36] however, exhibit a discrepancy by a factor of 10, probably due to the different reaction temperature and the platinum promotion. The somewhat higher CTY for the reference material Co/$\alpha$-$Al_2O_3$ can be explained by the smaller cobalt particle sizes and agrees with previously reported values.[42] The TOF values determined at a reaction temperature of 240 °C are almost proportional to the CTY since the cobalt particle size is similar for all materials except Co/$\alpha$-$Al_2O_3$. The comparison to the latter material as reference exhibits reasonable FT active catalysts.

The apparent activation energy is found to be in the range expected for intrinsic conditions in FT reaction being in the order of 120 $kJ\,mol^{-1}$,[59,60] thus pronounced mass transfer limitations can be ruled out. In contrast, the TOF exhibits a difference by a factor of two among the zeolitic materials studied. This points at an impact of the zeolite nature, in particular pore structure and acidity, on the catalytic activity of the Co nanoparticles, which is underlined by the even more pronounced difference to the Co@$mSiO_2$ material. In order to unravel the respective mechanism, further research is required, though. The progress of the CTY over time on stream (TOS) indicates a slight decrease, which is more pronounced at 260 °C (see SI, Figure S14). Additionally, no significant change of the methane selectivity over the last 36 h of the FT experiment is detected. Significant growth of the cobalt particles during FT reaction can be ruled out as revealed by TEM analysis of spent catalyst (see SI, Figure S16 and S17). Other sources of catalyst deactivation could be cobalt oxidation and coking.[61,62]

Figure 5 provides the relative hydrocarbon selectivities at two different reaction temperatures (240 and 260 °C) of the catalyst materials Co@$mSiO_2$, Co@silicalite-1-HT, Co@HZSM5-HT, Co@mHZSM5-HT, Co@HZSM5-SAC and Co/$\alpha$-$Al_2O_3$ compared on basis of the descriptors PS and AC normalized to CSA. Note that the conversion of each material differs to a certain extent, which may also affect the observed selectivities. We, therefore, discuss the general trend in selectivity, rather than absolute values. The AC/CSA value is increasing from left to right until Co@mHZSM5-HT, while Co@HZSM5-SAC shows the same value as Co@silicalite-1-HT. The PS/CSA is the highest for Co@$mSiO_2$ and also increases from left to right among the zeolitic materials to Co@mHZSM5-HT, while Co@HZSM5-SAC shows a slightly lower value than Co@mHZSM5-HT. Since the $CO_2$

**Table 6.** CO conversion ($X_{CO}$), cobalt time yield (***CTY***) and turn over frequency (***TOF***) of the catalyst materials at 240 and 260 °C.[a]

| *T* [°C] | Catalyst | $X_{CO}$ [%] | *CTY* [$10^{-5}$ $mol_{CO}$ $g_{Co}^{-1}$ $s^{-1}$] | *TOF* [$10^{-3}$ $s^{-1}$] |
|---|---|---|---|---|
| 240 | Co@$mSiO_2$ | 21.1 | 7.60 | 142 |
| | Co@silicalite-1-HT | 33.2 | 6.60 | 116 |
| | Co@HZSM5-HT | 9.4 | 2.70 | 44 |
| | Co@mHZSM5-HT | 27.5 | 5.50 | 90 |
| | Co@HZSM5-SAC | 19.1 | 6.00 | 104 |
| | Co/$\alpha$-$Al_2O_3$ | 12.2 | 11.70 | 72 |
| 260 | Co@$mSiO_2$ | 15.0 | 22.20 | 416 |
| | Co@silicalite-1-HT | 22.4 | 16.90 | 297 |
| | Co@HZSM5-HT | 8.2 | 8.90 | 145 |
| | Co@mHZSM5-HT | 22.4 | 16.30 | 268 |
| | Co@HZSM5-SAC | 14.6 | 16.30 | 283 |

[a] reaction conditions: p = 20 bar, $H_2$/CO = 2, gas hourly space velocity (GHSV) 3 $m^3\ kg_{cat}^{-1}\ h^{-1}$ for 240 °C and 13 $m^3\ kg_{cat}^{-1}\ h^{-1}$ for 260 °C, as well as 20 $m^3\ kg_{cat}^{-1}\ h^{-1}$ for Co/$\alpha$-$Al_2O_3$; all values determined after 55 h time on stream (TOS).

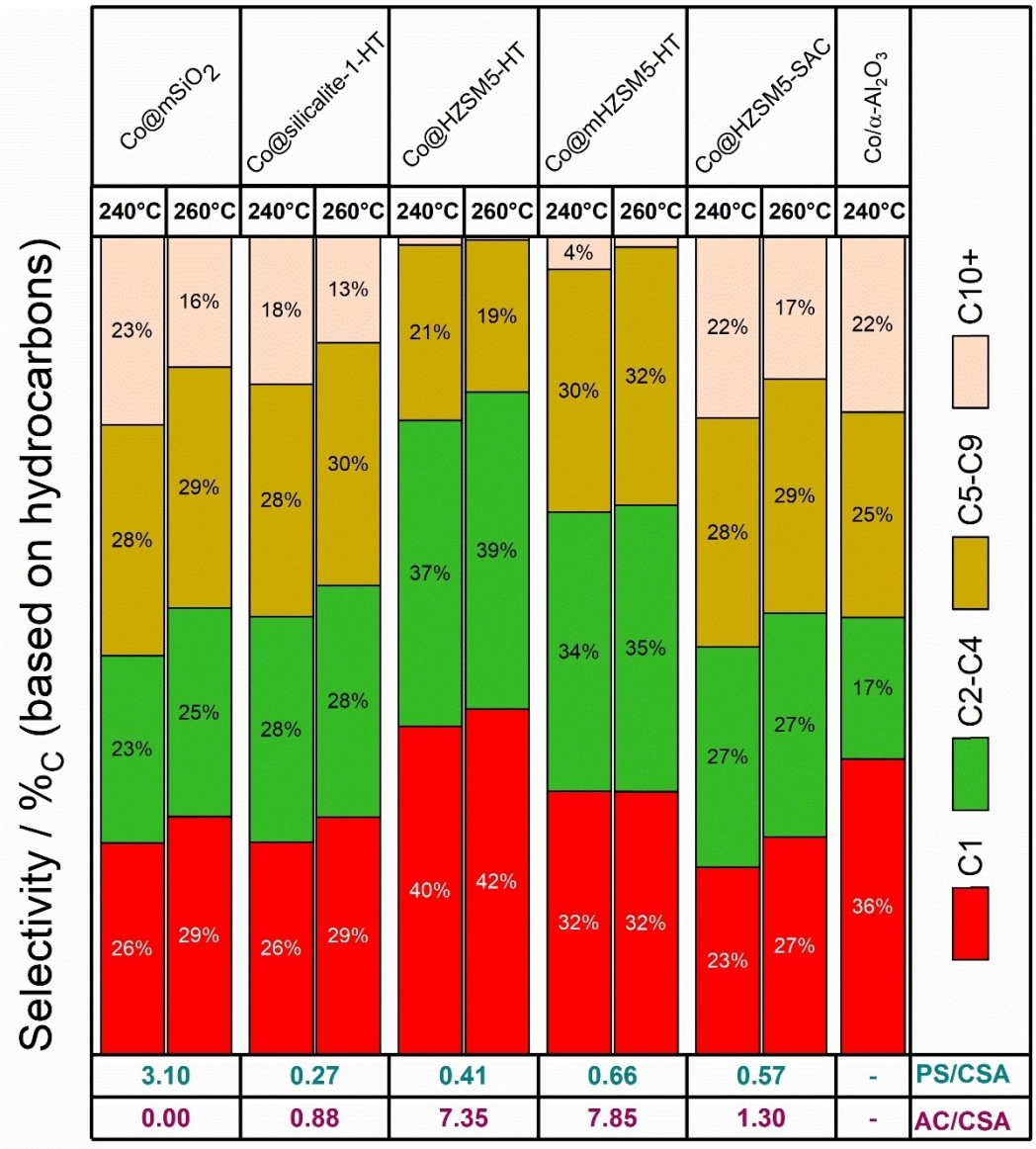


**Figure 5.** Hydrocarbon selectivities of Co@mSiO$_2$, Co@silicalite-1-HT, Co@HZSM5-HT, Co@mHZSM5-HT, Co@HZSM5-SAC and Co/α-Al$_2$O$_3$ at 240 and 260 °C as function of descriptors for pore structure (PS) and acidity (AC) normalized to cobalt surface area (CSA); not considered are selectivity values lower 3%; values determined after 55 h TOS.

selectivity is below 5% or even smaller in all cases, it will not be considered in detail for discussion of hydrocarbon selectivities (see SI, Tab. S4). The corresponding formation rates for the different hydrocarbon fractions are provided in Table S5 (see SI).

The methane selectivity in Figure 5 (C1 fraction in red) for Co@mSiO$_2$, Co@silicalite-1-HT, and Co@HZSM5-SAC is in the range of 20 to 30% with slightly higher values at 260 °C, which is in reasonable agreement with literature data for comparable materials.[17,63] Both HZSM-5 materials, Co@HZSM5-HT and Co@mHZSM5-HT, however, show rather high methane selectivities in the range of 30 to 40%. Importantly, those values are comparable to that found for the reference material (Co/α-Al$_2$O$_3$) at 240 °C, which underlines the consistency of the observed selectivities. Note that for the reference material a methane selectivity of 10.9% at 220 °C was reported earlier.[42] The high methane selectivity at those temperatures is not surprising and frequently reported in the literature.[64–67] For Co/ZSM5 materials, in particular, Carvalho et al.[36] and Flores et al.[35] report values of up to 28% or even 37% at 250 °C, while Sartipi et al.[68] and Cheng et al.[69] observed ca. 23% at 240 °C. Although the estimated apparent activation energy indicates no strong impact of mass transfer limitations of zeolitic materials a certain effect might retain, which could cause a locally increased H$_2$:CO ratio and therefore the preferential formation of methane.[70,71] Co@mSiO$_2$ and Co@silicalite-1-HT, however, reveal similar methane selectivities, with both materials consisting of SiO$_2$ and differing only by crystallinity and pore size. Therefore, a locally increased H$_2$:CO ratio induced by diffusion limitation in microporous Co@silicalite-1-HT is unlikely,

as this would lead to an increase in methane selectivity.[64] This is in contrast to the comparison between Co@HZSM5-HT and Co@mHZSM5-HT, where the latter exhibits additional mesopores. Obviously and in agreement with Flores et al.,[35] the methane selectivity is lower, if mesopores are present, which indicates a locally higher $H_2$:CO ratio for Co@HZSM5-HT. An additional factor contributing to an increased methane selectivity is the hydrogenolysis of preferably heavier paraffins taking place on group VIII metals like cobalt, which causes successive demethylation at the end of the hydrocarbon chain-forming methane and a heavier fragment.[72,73] While this effect is reported to be smaller over catalysts with larger cobalt particle sizes, it is very likely to occur at the presented materials. Interestingly, the comparison of Co@HZSM5-HT and Co@silicalite-1-HT, reveals a significantly lower methane selectivity for the latter case, even though the pore structure and cobalt particle size are comparable. The only difference is the presence of acidic sites in Co@HZSM5-HT in close proximity of the FT active cobalt particles, while for the Co@mHZSM5-HT catalyst the diffusion limitation effect is probably less pronounced, which leads to a decrease in methane selectivity. Therefore, the increased methane selectivity for Co@HZSM5-HT might not necessarily be caused be diffusion limitations of the reactants, but probably of the products. In other words, the diffusion restrictions through the microporous zeolite increases the residence time of the formed hydrocarbons in proximity of the cobalt nanoparticle, which may support methane formation by hydrogenolysis.

Comparing Co@m$SiO_2$ and Co@silicalite-1-HT on basis of the other C-fractions a slightly higher selectivity towards $C_2$–$C_4$ and $C_5$–$C_9$ for Co@silicalite-1-HT as well as a reduced $C_{10+}$ selectivity can be found. This points towards a marginally hindered diffusion of larger $C_{10+}$ product molecules through the microporous structure. This observation was already reported by Subramanian et al. as they found a limitation of chain growth in zeolite pores resulting in non-linear ASF distribution.[40] The comparison between the materials Co@silicalite-1-HT and Co@HZSM5-HT reveals a strongly reduced selectivity for the $C_5$–$C_9$ and $C_{10+}$ fraction, while it is higher for the $C_2$–$C_4$ fraction for Co@HZSM5-HT. The shift from $C_{5+}$ to the $C_2$–$C_4$ fraction can be explained by cracking at the acidic sites present in Co@HZSM5-HT, as indicated by the AC/CSA descriptor. Since the C–C scission takes place rather central of aliphatic hydrocarbons, one cracked molecule forms two hydrocarbons with similar chain length.[74] The described observations are more pronounced at higher temperatures due to an increased cracking reaction rate. Note that the acidity, as expressed by the AC/CSA ratio, of Co@HZSM5-HT and Co@mHZSM5-HT is similar, while the PS/CSA descriptor for Co@mHZSM5-HT is higher. The improved diffusive transport within the porous structure of Co@mHZSM5-HT also explains the higher $C_{10+}$ fraction compared to Co@HZSM5-HT, since overcracking is reduced by short contact times.[35,36] The higher content of the intermediate fraction ($C_5$–$C_9$) can also be explained by mass transport effects. Those species are formed by chain growth during FT reaction, but also by C–C-scissions of longer hydrocarbon chains diffusing through the microporous structure. Since diffusion coefficients are higher for smaller hydrocarbons,[75] the $C_5$–$C_9$ molecules formed by cracking are able to leave the proximity of acidic sites faster, which reduces the cracking probability of the respective molecules. Similar observations for mesoporous zeolites were also reported by Cheng et al.[69] It is noteworthy, that the descriptor PS/CSA is based on the mesopore volume only, without information on the specific diffusion path in the hierarchical pore structures present in Co@mHZSM5-HT. Thus, the impact of individual transport trajectories of the FT products on the cracking probability is not derivable. The Co@HZSM5-SAC catalyst material shows the same AC/CSA value as Co@silicalite-1-HT, but the PS/CSA is somewhat higher. Note, that the zeolite crystals of Co@HZSM5-SAC are larger (about 5 μm) than the ones of Co@silicalite-1-HT (1 μm). Due to the larger crystal size and therefore higher diffusion length of Co@HZSM5-SAC, the FT reaction is probably mainly taking place on cobalt particles at the zeolite surface. Thus, no diffusion limitations are contributing since the FT products preferably diffuse along the external surface of the zeolite crystals. The selectivities towards $C_2$–$C_4$ and $C_5$–$C_9$ fractions of Co@HZSM5-SAC are comparable to Co@silicalite-1-HT. Interestingly, the selectivity to the $C_{10+}$ fraction for Co@HZSM5-SAC is higher compared to Co@silicalite-1-HT. Presumably, because of the reaction mainly taking place at the outer zeolite surface, larger hydrocarbons can be formed more easily. In contrast, the reference material Co/α-$Al_2O_3$ exhibits the lowest selectivity to the $C_2$–$C_4$ fraction compared to all catalyst materials, while the selectivities towards the $C_5$–$C_9$ and $C_{10+}$ fractions are almost comparable to Co@HZSM5-SAC, probably due to the absence of diffusion limitations.

Figure 6 provides the production rates of n-paraffins, 1-olefins, and paraffinic and olefinic isomers in the $C_2$–$C_4$ and $C_5$–$C_9$ fractions, as well as the $C_{10+}$ fraction at a reaction temperature of 260 °C (see SI, Figure S15 for 240 °C). The $C_{10+}$ fraction represents the respective heavier paraffins, olefins, and isomers since a distinction by GC analysis would be too time-intensive. This fraction is indispensable for discussion since it represents the source for the $C_5$–$C_9$ fraction whenever cracking reactions are occurring. The arrangement of materials Co@m-$SiO_2$, Co@silicalite-1-HT, Co@HZSM5-HT, Co@mHZSM5-HT, and Co@HZSM5-SAC and thus the order of the descriptors PS/CSA and AC/CSA is identical to Figure 5.

Co@m$SiO_2$ exhibits high n-paraffin formation rates for both the $C_2$–$C_4$ and the $C_5$–$C_9$ fraction. The comparison of both fractions with respect to 1-olefin and isomer formation rates, however, provide significantly different behaviors. While in the $C_2$–$C_4$ fraction the isomer content is low, since the number of isomers contributing to this fraction is low, the 1-olefin formation in the $C_5$–$C_9$ fraction is minorly expressed. The relatively high isomer content in the $C_5$–$C_9$ fraction is surprising since no acidic sites are observed (AC/CSA = 0), responsible for the isomerization of linear hydrocarbons. One of the reasons for the high isomer-to-olefin ratio could be transport restrictions of the products through the mesoporous shell, which increases the 1-olefin residence time in the proximity of active cobalt particles and thus facilitates olefin readsorption and subsequent

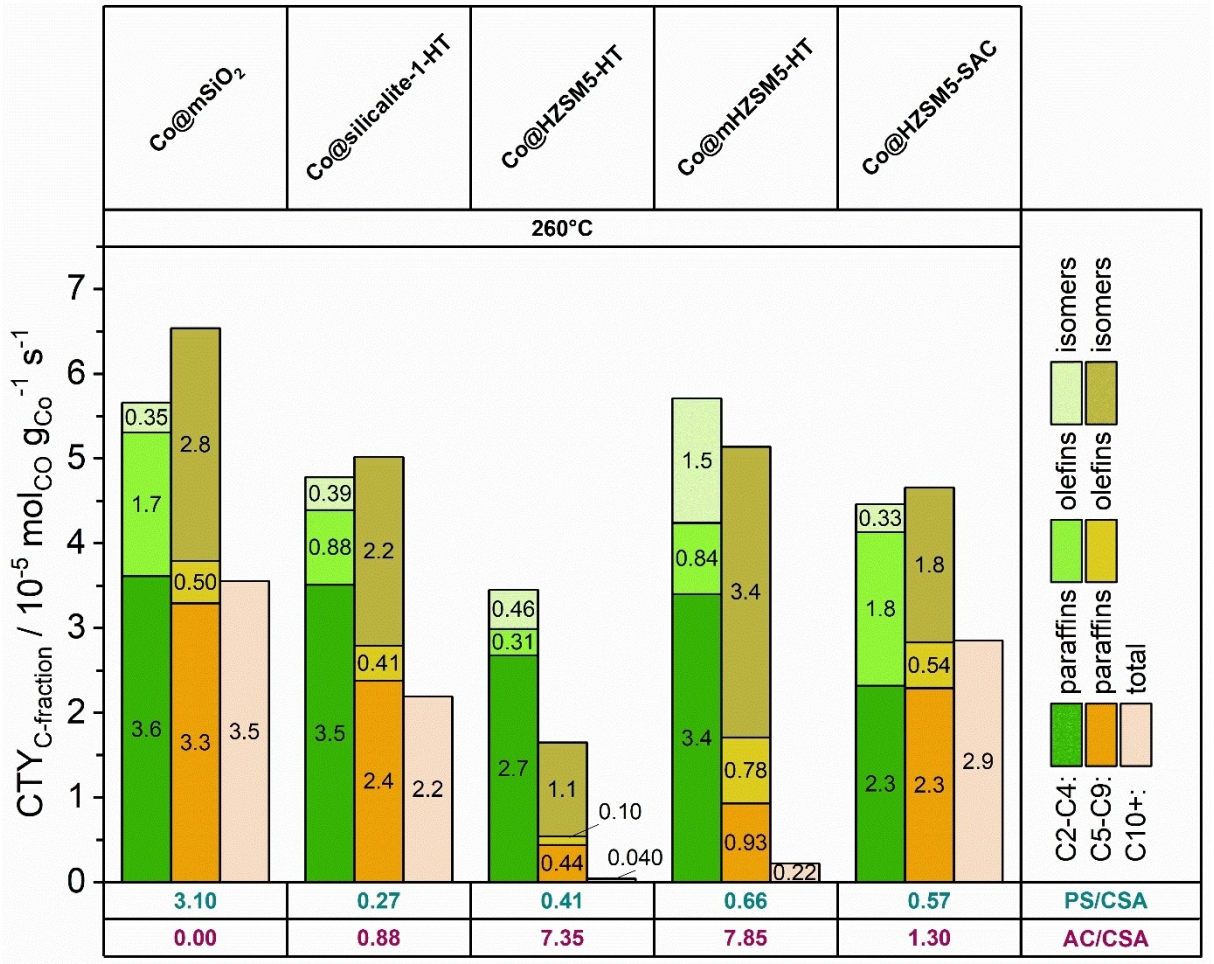


**Figure 6.** n-Paraffin, 1-olefin and isomer (olefins + paraffins) formation rates of the $C_2$-$C_4$ and $C_5$-$C_9$ fraction for Co@mSiO$_2$, Co@silicalite-1-HT, Co@HZSM5-HT, Co@mHZSM5-HT and Co@HZSM5-SAC at 260 °C as a function of descriptors for pore structure (PS) and acidity (AC) normalized to cobalt surface area (CSA); the numbers in the bars represent the formation rate of the respective hydrocarbon compound.

secondary reactions, such as hydrogenation to paraffins.[35] Furthermore, an increasing residence time near acidic sites leads to a higher probability of isomer formation, as well. This effect is more pronounced for the $C_5$–$C_9$ fraction since diffusive transport is improved for shorter hydrocarbon chains.[75] The relative selectivity values reflect the trend of the formation rates of the C-fractions (see SI, Table S4). Note, compared to all catalysts Co@mSiO$_2$ displays the highest formation rate for the $C_{10+}$ fraction.

A comparable composition of hydrocarbon products can be found for Co@silicalite-1-HT, whereas the detected formation rates are slightly lower than for Co@mSiO$_2$. Both materials are based on SiO$_2$ with low or no acidity and differ in pore structure only. Co@silicalite-1-HT offers micropores showing a ten times lower PS/CSA descriptor than Co@mSiO$_2$. Hence, the lower hydrocarbon formation rate can most probably be ascribed to the sieve effect or to slight diffusion restrictions present for the microporous material, especially for the $C_{5+}$ products. The $C_2$–$C_4$ fraction of Co@silicalite-1-HT exhibits a lower formation rate to 1-olefins than Co@mSiO$_2$, while in the $C_5$–$C_9$ fraction a lower formation rate to n-paraffins is found, even if the olefin-to-paraffin ratio is not changing. Thus, the above-mentioned higher olefin readsorption probability seems to be more pronounced for Co@silicalite-1-HT as well. The relative selectivity values are comparable to the ones of Co@mSiO$_2$ (see SI, Table S4).

Co@HZSM5-HT, providing acidic sites for cracking and isomerization (AC/CSA = 7.35), exhibits a high n-paraffin content in the $C_2$–$C_4$ fraction, a high isomer content in the $C_5$-$C_9$ fraction, and a negligible $C_{10+}$ content (for relative selectivity values see SI, Tab. S4). This observation, compared to the non-acidic material Co@silicalite-1-HT, indicates cracking and isomerization reactions are occurring at the acidic material in addition to the above-mentioned secondary reactions. Note that both materials exhibit similar pore structure (PS/CSA are similar) and thus comparable restrictions in diffusive transport, which affects both primary and secondary cracking/isomerization reactions in zeolite materials.[76] The small 1-olefin content could be explained by the $C_2$–$C_4$ olefin oligomerization over acidic sites leading to the formation of isomers under FT conditions.[40,77] Furthermore, a significant amount of isomers is probably produced by olefin isomerization at acid sites directly,[35,36]

which is supported by the high isomer-to-olefin ratio found for Co@HZSM5-HT. The high n-paraffin content in the $C_2$–$C_4$ fraction can be explained by an increased rate of 1-olefin secondary hydrogenation leading to higher n-paraffin yields.[35] The small formation rates of $C_{5+}$ species support the occurrence of overcracking/secondary cracking, as already discussed above.[36,69] Thus, the residence time of the hydrocarbon products in the microporous zeolite matrix appears to play an important role, in addition to the acidity.[78]

The leached zeolite material Co@mHZSM5-HT exhibits the highest hydrocarbon formation rate after Co@m$SiO_2$. The $C_2$–$C_4$ and $C_5$–$C_9$ fractions are almost formed in similar amounts. Therefore, the distribution among the fractions differs strongly from Co@HZSM5-HT, where the $C_2$–$C_4$ fraction is mainly formed. In contrast, the distribution within the fractions is rather similar for both materials Co@HZSM5-HT and Co@mHZSM5-HT, being n-paraffins the main product in $C_2$–$C_4$ and isomers in the $C_5$–$C_9$ fraction. A closer look (see SI, Tab. S4), however, reveals for Co@mHZSM5-HT a lower n-paraffin and a higher isomer content in the $C_2$–$C_4$ fraction, as well as a higher $C_5$–$C_9$ 1-olefin content. Consequently, cracking and isomerization reactions occur similarly in both materials Co@HZSM5-HT and Co@mHZSM5-HT given by the comparable acidity of both materials. The higher PS/CSA value of Co@mHZSM5-HT, however, provides the products to be transported faster through the zeolite structure. Therefore, overcracking is avoided and the isomerization probability is increasing, in addition, secondary reactions of olefins are less likely.[36,69] To decrease diffusion limitations and overcracking of long-chain hydrocarbons the development of hierarchical zeolite materials is the subject of many research groups.[18,79] As also shown by our work an enhanced selectivity towards the $C_5$–$C_9$ and $C_{10+}$ fraction can be achieved. But often the authors also reported the formation of a lower fraction of branched hydrocarbons, showing a ratio of isomers-to-paraffins usually close to unity.[18,79] This is not the case in our work, where isomer-to-paraffin ratios of 2.5 and 3.7 for Co@HZSM5-HT and Co@mHZSM5-HT, respectively, are observed in the $C_5$–$C_9$ fraction at 260 °C probably because of olefin oligomerization taking place.

For Co@HZSM5-SAC the overall formation rate is slightly lower than for Co@silicalite-1-HT. A closer look at the different hydrocarbon fractions reveals a more comparable behavior to Co@m$SiO_2$. In particular, high n-paraffin formation rates for both the $C_2$–$C_4$ and the $C_5$–$C_9$ fraction are detected, while the formation rate towards $C_{10+}$ products is high, too. The comparison of the $C_2$–$C_4$ and the $C_5$–$C_9$ fractions with respect to 1-olefin and isomer formation rates provides a higher 1-olefin content in $C_2$–$C_4$ as well a relatively high isomer content in the $C_5$–$C_9$ fraction. The generally high n-paraffin formation rate and formation of heavier hydrocarbons probably result from the increased diffusion length through the zeolite crystals (5 μm) and therefore as a result the FT reaction is mainly taking place at the external zeolite surface as already discussed above.

The corresponding results at a reaction temperature of 240 °C (see SI, Figure S15) show a less pronounced impact of the cracking and isomerization reactions. In particular, the $C_{10+}$ formation rate is clearly higher for all catalyst materials since primary cracking reactions are less favored at lower reaction temperatures. The lower isomer content indicates less pronounced secondary cracking/isomerization reactions, as well. It has to be mentioned, however, that the influence of the acidic sites is still detectable by comparison of the $C_{10+}$ formation rate of the acidic and non-acidic materials.

In Figure 7 the rates for cracking, isomerization, and $C_{10+}$ formation are shown as a function of the AC/PS descriptor ratio. Obviously, the cracking rate increases with AC/PS ratio associated with a decreasing $C_{10+}$ formation rate, since long-chain hydrocarbons are more preferably cracked at acidic sites of the zeolite. It has to be mentioned that high AC/PS values indicate either high acidity or small mesopore volume. In other words, it expresses the ratio between cracking activity and diffusion rate. High AC/PS values, therefore, increase the residence time of hydrocarbons inside the zeolite matrix and the cracking activity at the same time, which eventually leads to an increased cracking probability. Following this argumentation, the maximum isomerization rate at AC/PS ≈ 12 indicates an optimal ratio between acidity and diffusion rate. Thus, isomers are formed at the acidic sites and are able to leave the zeolite by diffusion before being further converted at those sites. It has to be emphasized that hydrocarbons formed at the surface of non-encapsulated Co particles eventually also enter the pores of the zeolite, where cracking and isomerization takes place. Therefore, a clear effect of the AC/PS ratio on the cracking and isomerization rates can be observed, though partial Co particle encapsulation within the zeolite matrix is achieved only.

The observations in this work thus fit with the conclusions drawn in the literature. Co@HZSM5-HT exhibits low isomer and $C_{5+}$ selectivity due to secondary hydrogenation and over-

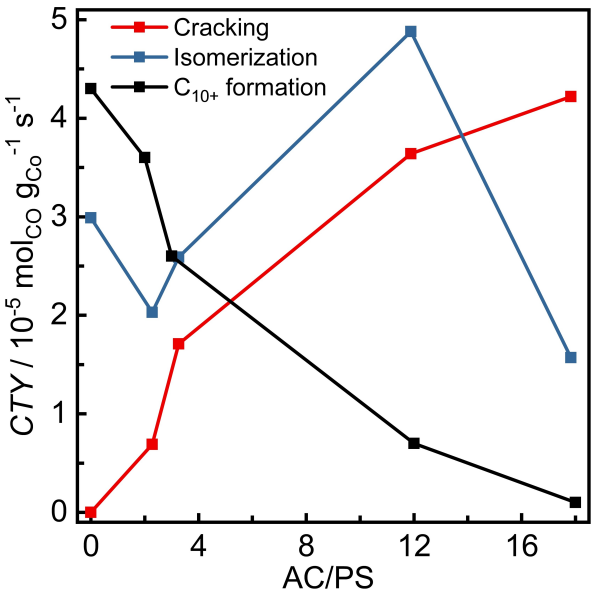


**Figure 7.** Rates for cracking ($\Delta CTY_{10+}$), isomerization ($CTY_{iso}$) and $C_{10+}$ formation ($CTY_{10+}$) as function of AC/PS ratio for Co@m$SiO_2$ (AC/PS = 0), Co@HZSM5-SAC (AC/PS = 2.28), Co@silicalite-1-HT (AC/PS = 3.26), Co@mHZSM5-HT (AC/PS = 11.89) and Co@HZSM5-HT (AC/PS = 17.83); definition of rates see SI.

cracking induced by diffusion restrictions. In contrast, the additional porosity in Co@mHZSM5-HT leads to an increased isomer and $C_{5+}$ selectivity as a result of improved diffusive transport and short contact times.[35,36] Since the diffusion coefficients are higher for smaller hydrocarbons,[75] the $C_5$–$C_9$ molecules formed by cracking are able to leave the proximity of acidic sites faster, which reduces the cracking probability of respective molecules. Similar observations for mesoporous zeolites are also reported by Cheng et al.[69]

## Conclusions

In this work, we applied the bottom-up synthesis strategy for bifunctional cobalt-zeolite catalysts with different acidity and porosity in order to study their performance in the combined FT and HP reactions. Therefore, cobalt nanoparticles of comparable sizes in the range of 25 to 30 nm were prepared prior to the stepwise synthesis of bifunctional cobalt-zeolite materials. The cobalt mass loadings between 5 and 8% determined via TPR and ICP are in good agreement. The modification of the micropore structure of the zeolite crystals with additional mesopores was achieved by base leaching. The catalytic materials are fully characterized with emphasis on the cobalt surface area (CSA), the pore structure (PS), and the acidity (AC). Those easily accessible characterization results were used for defining the respective descriptors representing the FT activity, the transport rate through the porous structure, as well as the hydroprocessing activity. Since the descriptor for FT activity is kept constant, the obtained product spectrum can be correlated to the pore structure and acidity, directly. The bifunctional cobalt-zeolite materials were further characterized by 3D TEM tomography in order to evaluate the degree of encapsulation found to be about 25–30%. The investigation of the hierarchical pore structure after base leaching of the zeolite crystal reveals the formation of a cavity in the center of the zeolite crystal, while the cobalt particles can be stabilized through mesopores inside the cavity.

Catalytic experiments are performed for the investigation of the product distribution in the combined FT and HP reactions. It is observed that the pore structure and the acidity, characterized by the normalized descriptors PS/CSA and AC/CSA, affect the chain length distribution and the composition of the product spectrum significantly. While the acidity majorly causes primary cracking/isomerization reactions, the porosity affects secondary isomerization. In particular, olefin readsorption in the $C_5$-$C_9$ fraction and cracking of $C_{10+}$ hydrocarbons appear to be facilitated by restricted diffusion in microporous structures. Therefore, the particular 3D pore structure and thus the individual transport trajectories of the FT products is strongly affecting the cracking probability. The acidity, however, mainly affects the $C_{10+}$ formation rate, due to the related cracking activity. The observations thus reveal that the pore structure appears to play a vital role in primary and secondary cracking/isomerization reactions. Hence, particular emphasis should be given to the pore structure and not only to acidity for tailoring the product distribution in combined FT/HP reaction in future work. In addition, descriptors provide a powerful tool for catalyst parameter testing and correlation to FT product distribution. This approach can optimize future research studies to identify suitable catalysts more easily.

## Acknowledgements

*The authors would like to thank Kang Cheng and Jogchum Oenema from ICC of Utrecht University for $NH_3$-TPD measurements. László Eifert from Helmholtz Institute Ulm is kindly thanked for the powder X-ray diffraction and the SEM measurements. Angela Straß-Eifert acknowledges the Travel grant from the Subject Division "Reaction Engineering" of ProcessNet. Open access funding enabled and organized by Projekt DEAL.*

## Conflict of Interest

The authors declare no conflict of interest.

**Keywords:** Bifunctional catalyst · Cobalt · Fischer Tropsch synthesis · Heterogeneous catalysis · Supported catalysts

[1] C. Le Quéré, et al., *Earth Syst. Sci. Data* **2015**, *7*, 349–396.
[2] United Nations, "The Paris Agreement", to be found under https://unfccc.int/process-and-meetings/the-paris-agreement/the-paris-agreement, **2015**.
[3] Federal Ministry for Economic Affairs and Energy (BMWi), "Renewable Energy Source in Figures. National and International Development, 2017", to be found under https://www.bmwi.de/Redaktion/EN/Publikationen/renewable-energy-sources-in-figures-2017.html, **2018**.
[4] ProcessNet-Arbeitsausschuss "Alternative flüssige und gasförmige Kraft- und Brennstoffe", "Advanced alternative liquid fuels: For climate protection in the global raw materials change", to be found under https://dechema.de/dechema_media/Downloads/Positionspapiere/2018_alternativeBrennstoffe_en.pdf, **2018**.
[5] M. Loewert, P. Pfeifer, *Chem. Eng.* **2020**, *4*, 21.
[6] R. Güttel, T. Turek, *Energy Technol.* **2016**, *4*, 44–54.
[7] D. X. Martínez-Vargas, L. Sandoval-Rangel, O. Campuzano-Calderon, M. Romero-Flores, F. J. Lozano, K. D. P. Nigam, A. Mendoza, A. Montesinos-Castellanos, *Ind. Eng. Chem. Res.* **2019**, *58*, 15872–15901.
[8] T. Jermwongratanachai et al., *Appl. Catal. A.* **2013**, *464–465*, 165–180.
[9] P. Munnik, P. E. de Jongh, K. P. de Jong, *J. Am. Chem. Soc.* **2014**, *136*, 7333–7340.
[10] E. Rytter, Ø. Borg, N. E. Tsakoumis, A. Holmen, *J. Catal.* **2018**, *365*, 334–343.
[11] Q. Zhang, J. Kang, Y. Wang, *ChemCatChem* **2010**, *2*, 1030–1058.
[12] J. Liu, D. Wang, J.-F. Chen, Y. Zhang, *Int. J. Hydrogen Energy* **2016**, *41*, 21965–21978.
[13] R. Yang, L. Zhou, J. Gao, X. Hao, B. Wu, Y. Yang, Y. Li, *Catal. Today* **2017**, *298*, 77–88.
[14] C. Sun, P. Pfeifer, R. Dittmeyer, *Chem. Eng. J.* **2017**, *326*, 37–46.
[15] S. Bessell, *Appl. Catal. A.* **1995**, *126*, 235–244.
[16] A. Martínez, J. Rollán, M. A. Arribas, H. S. Cerqueira, A. F. Costa, E. F. S.-Aguiar, *J. Catal.* **2007**, *249*, 162–173.
[17] S.-H. Kang, J.-H. Ryu, J.-H. Kim, P. S. Sai Prasad, J. W. Bae, J.-Y. Cheon, K.-W. Jun, *Catal. Lett.* **2011**, *141*, 1464–1471.
[18] S. Sartipi, M. Alberts, M. J. Meijerink, T. C. Keller, J. Pérez-Ramírez, J. Gascon, F. Kapteijn, *ChemSusChem* **2013**, *6*, 1646–1650.
[19] C. Zhu, G. M. Bollas, *Appl. Catal. B* **2018**, *235*, 92–102.
[20] J. H. Lee, W. Bonte, S. Corthals, F. Krumeich, M. Ruitenbeek, J. A. van Bokhoven, *Ind. Eng. Chem. Res.* **2019**, *58*, 5140–5145.
[21] W. Li, Y. He, H. Li, D. Shen, C. Xing, R. Yang, *Catal. Commun.* **2017**, *98*, 98–101.
[22] H. Becker, R. Güttel, T. Turek, *Chem. Ing. Tech.* **2014**, *86*, 544–549.

[23] K. P. de Jong, J. Zečević, H. Friedrich, P. E. de Jongh, M. Bulut, S. van Donk, R. Kenmogne, A. Finiels, V. Hulea, F. Fajula, *Angew. Chem. Int. Ed.* **2010**, *49*, 10074–10078; *Angew. Chem.* **2010**, *122*, 10272–10276.
[24] A. Freitez, K. Pabst, B. Kraushaar-Czarnetzki, G. Schaub, *Ind. Eng. Chem. Res.* **2011**, *50*, 13732–13741.
[25] K. Pabst, B. Kraushaar-Czarnetzki, G. Schaub, *Ind. Eng. Chem. Res.* **2013**, *52*, 8988–8995.
[26] A. M. Subiranas, G. Schaub, *Int. J. Chem. React. Eng.* **2007**, *A78*.
[27] A. M. Subiranas, G. Schaub, *Int. J. Chem. React. Eng.* **2009**, *A31*, 1–24.
[28] C. Sun, M. Klumpp, J. R. Binder, P. Pfeifer, R. Dittmeyer, *Chem. Ing. Tech.* **2017**, *89*, 894–902.
[29] X. Li, J. He, M. Meng, Y. Yoneyama, N. Tsubaki, *J. Catal.* **2009**, *265*, 26–34.
[30] Y. Li, T. Wang, C. Wu, Y. Lv, N. Tsubaki, *Energy Fuels* **2008**, *22*, 1897–1901.
[31] J. Bao, J. He, Y. Zhang, Y. Yoneyama, N. Tsubaki, *Angew. Chem. Int. Ed.* **2008**, *47*, 353–356; *Angew. Chem.* **2008**, *120*, 359–362.
[32] G. Yang, C. Xing, W. Hirohama, Y. Jin, C. Zeng, Y. Suehiro, T. Wang, Y. Yoneyama, N. Tsubaki, *Catal. Today* **2013**, *215*, 29–35.
[33] M. Javed, S. Cheng, G. Zhang, P. Dai, Y. Cao, C. Lu, R. Yang, C. Xing, S. Shan, *Fuel* **2018**, *215*, 226–231.
[34] S. Sartipi, J. E. van Dijk, J. Gascon, F. Kapteijn, *Appl. Catal. A.* **2013**, *456*, 11–22.
[35] C. Flores, N. Batalha, V. V. Ordomsky, V. L. Zholobenko, W. Baaziz, N. R. Marcilio, A. Y. Khodakov, *ChemCatChem* **2018**, *10*, 2291–2299.
[36] A. Carvalho, M. Marinova, N. Batalha, N. R. Marcilio, A. Y. Khodakov, V. V. Ordomsky, *Catal. Sci. Technol.* **2017**, *7*, 5019–5027.
[37] N. Kruse, A. G. Machoke, W. Schwieger, R. Güttel, *ChemCatChem* **2015**, *7*, 1018–1022.
[38] X. Zhu et al., *Nat. Commun.* **2019**, *10*, 1428.
[39] L. Pirro, P. S. F. Mendes, S. Paret, B. D. Vandegehuchte, G. B. Marin, J. W. Thybaut, *Catal. Sci. Technol.* **2019**, *9*, 3109–3125.
[40] V. Subramanian, K. Cheng, C. Lancelot, S. Heyte, S. Paul, S. Moldovan, O. Ersen, M. Marinova, V. V. Ordomsky, A. Y. Khodakov, *ACS Catal.* **2016**, *6*, 1785–1792.
[41] A. G. Machoke, A. M. Beltrán, A. Inayat, B. Winter, T. Weissenberger, N. Kruse, R. Güttel, E. Spiecker, W. Schwieger, *Adv. Mater.* **2015**, *27*, 1066–1070.
[42] C. Hernández Mejía, T. W. van Deelen, K. P. de Jong, *Nat. Commun.* **2018**, *9*, 4459.
[43] J. Schindelin et al., *Nat. Methods* **2012**, *9*, 676–682.
[44] R. Krishna, J. A. Wesselingh, *Chem. Eng. Sci.* **1997**, *52*, 861–911.
[45] J. L. Anderson, J. A. Quinn, *Biophys. J.* **1974**, 130–150.
[46] J. Kremer, D. N. Mastronarde, J. R. McIntosh, *J. Struct. Biol.* **1996**, *116*, 71–76.
[47] J. Ilsemann, A. Straß-Eifert, J. Friedland, L. Kiewidt, J. Thöming, M. Bäumer, R. Güttel, *ChemCatChem* **2019**, *11*, 4884–4893.
[48] A. Straß-Eifert, T. L. Sheppard, C. D. Damsgaard, J.-D. Grunwaldt, R. Güttel, *ChemCatChem* **2021**, *13*, 718–729.
[49] G. L. Bezemer, J. H. Bitter, H. P. C. E. Kuipers, H. Oosterbeek, J. E. Holewijn, X. Xu, F. Kapteijn, A. J. van Dillen, K. P. de Jong, *J. Am. Chem. Soc.* **2006**, *128*, 3956–3964.
[50] G. Jacobs, T. K. Das, Y. Zhang, J. Li, G. Racoillet, B. H. Davis, *Appl. Catal. A.* **2002**, 263–281.
[51] N. V. Beznis, B. M. Weckhuysen, J. H. Bitter, *Catal. Lett.* **2010**, *136*, 52–56.
[52] C. Ciotonea, B. Dragoi, A. Ungureanu, A. Chirieac, S. Petit, S. Royer, E. Dumitriu, *Chem. Commun.* **2013**, *49*, 7665–7667.
[53] X. Li, Y. Chen, M. U. Nisa, Z. Li, *Appl. Catal. B* **2020**, *267*, 118377.
[54] B. Jongsomjit, J. Panpranot, J. G. Goodwin, *J. Catal.* **2001**, *204*, 98–109.
[55] S. Svelle, L. Sommer, K. Barbera, P. N. R. Vennestrøm, U. Olsbye, K. P. Lillerud, S. Bordiga, Y.-H. Pan, P. Beato, *Catal. Today* **2011**, *168*, 38–47.
[56] N.-Y. Topsoe, K. Pedersen, E. G. Derouane, *J. Catal.* **1981**, *70*, 41–52.
[57] C. V. Hidalgo, H. Itoh, T. Hattori, M. Niwa, Y. Murakami, *J. Catal.* **1984**, *85*, 362–369.
[58] C. J. H. Jacobsen, C. Madsen, T. V. W. Janssens, H. J. Jakobsen, J. Skibsted, *Microporous Mesoporous Mater.* **2000**, 393–401.
[59] K. C. McMahon, S. L. Suib, B. G. Johnson, C. H. Bartholomew, *J. Catal.* **1987**, 47–53.
[60] M. F. M. Post, A. C. van't Hoog, J. K. Minderhoud, S. T. Sie, *AlChE J.* **1989**, *7*, 1107–1114.
[61] N. E. Tsakoumis, M. Rønning, Ø. Borg, E. Rytter, A. Holmen, *Catal. Today* **2010**, *154*, 162–182.
[62] N. E. Tsakoumis, J. C. Walmsley, M. Rønning, W. van Beek, E. Rytter, A. Holmen, *J. Am. Chem. Soc.* **2017**, *139*, 3706–3715.
[63] R. Xie, D. Li, B. Hou, J. Wang, L. Jia, Y. Sun, *Catal. Commun.* **2011**, *12*, 380–383.
[64] D. Vervloet, F. Kapteijn, J. Nijenhuis, J. R. van Ommen, *Catal. Sci. Technol.* **2012**, *2*, 1221.
[65] Z.-j. Wang, S. Skiles, F. Yang, Z. Yan, D. W. Goodman, *Catal. Today* **2012**, *181*, 75–81.
[66] H. Becker, R. Güttel, T. Turek, *Catal. Sci. Technol.* **2016**, *6*, 275–287.
[67] H. Becker, R. Güttel, T. Turek, *Catal. Sci. Technol.* **2019**, *9*, 2180–2195.
[68] S. Sartipi, K. Parashar, M. Makkee, J. Gascon, F. Kapteijn, *Catal. Sci. Technol.* **2013**, *3*, 572–575.
[69] K. Cheng, L. Zhang, J. Kang, X. Peng, Q. Zhang, Y. Wang, *Chem. Eur. J.* **2015**, *21*, 1928–1937.
[70] M. Kraum, M. Baerns, *Appl. Catal. A.* **1999**, 189–200.
[71] J. A. Lapszewicz, H. J. Loehn, J. R. Chipperfield, *J. Chem. Soc. Chem. Commun.* **1993**, 913–914.
[72] J. H. Sinfelt, *Adv. Catal.* **1973**, 91–119.
[73] X. Peng, K. Cheng, J. Kang, B. Gu, X. Yu, Q. Zhang, Y. Wang, *Angew. Chem. Int. Ed.* **2015**, *54*, 4553–4556; *Angew. Chem.* **2015**, *127*, 4636–4639.
[74] J. Weitkamp, *ChemCatChem* **2012**, *4*, 292–306.
[75] C. Erkey, J. B. Rodden, A. Akgerman, *Can. J. Chem. Eng.* **1990**, 661–665.
[76] S. van Donk, A. H. Janssen, J. H. Bitter, K. P. de Jong, *Catal. Rev.* **2003**, *45*, 297–319.
[77] R. J. Quann, L. A. Green, S. A. Tabak, F. J. Krambeck, *Ind. Eng. Chem. Res.* **1988**, 565–570.
[78] A. Corma, P. J. Miguel, A. V. Orchilles, *Appl. Catal. A.* **1994**, 29–40.
[79] K. Cheng, J. Kang, S. Huang, Z. You, Q. Zhang, J. Ding, W. Hua, Y. Lou, W. Deng, Y. Wang, *ACS Catal.* **2012**, *2*, 441–449.

Manuscript received: February 19, 2021
Revised manuscript received: March 23, 2021
Accepted manuscript online: April 7, 2021
Version of record online: May 4, 2021